PATIENT-SPECIFIC TECHNOLOGY FOR IN VIVO ASSESSMENT OF 3-D SPINAL MOTION

BY

JEREMY EDWARD GOODSITT

DISSERTATION

Submitted in partial fulfillment of the requirements
for the degree of Doctor of Philosophy in Mechanical Engineering
in the Graduate College of the
University of Illinois at Urbana-Champaign, 2017

Urbana, Illinois

Doctoral Committee:

Professor Iwona Jasiuk, Chair
Professor Avinash Patwardhan, Loyola University Chicago, Director of Research
Associate Professor Derek Hoiem
Assistant Professor Mariana Elizabeth Kersh

Abstract

One of the most common musculoskeletal problems affecting people is neck and low back pain. Traditional clinical diagnostic techniques such as fluoroscopic imaging or CT scans are limited due to their static and/or planar measurements which may not be able to capture all neurological pathologies. More advanced diagnostics have proven successful in assessing 3-D patient-specific spinal kinematics by combining a patient-specific 3-D spine model (CT or MRI) with bi-planar fluoroscopic imaging; however, custom, not clinically available advanced imaging equipment as well as an increase in radiation exposure is required to acquire a complete patient-specific spinal kinematic description. Hence, the purpose of this research was to develop a clinically viable bi-planar fluoroscopic imaging technique which acquires a complete patient-specific kinematic description of the spine with reduced radiation exposure.

Development of the proposed technique required evaluating the accuracy of 3-D kinematic interpolation techniques in reconstructing spinal kinematic data in order to reduce radiation exposure from bi-planar fluoroscopic diagnostic techniques. Several interpolation and sampling algorithms were evaluated in reconstructing cadaveric lumbar (L2-S1) flexion-extension motion data; ultimately, a new interpolation algorithm was proposed. Similarly, the success of the interpolation algorithm was evaluated in reconstructing spine-specific kinematic parameters.

Next, the interpolation algorithm was combined with a CT-based bi-planar fluoroscopic method. Accuracy of the proposed diagnostic technique was evaluated against previously validated work on an ex vivo optoelectronic 3-D kinematic assessment technique. Bi-planar fluoroscopic images were acquired during both flexion-extension and lateral bending motions of cadaveric cervical (C4-T1) and lumbar (L2-S1) spine. Registration of the bi-planar fluoroscopic images to the CT-based 3-D model was optimized using a gradient derived similarity function. Additionally, a stochastic approach, covariance matrix adaptive evolution strategy, was used as the optimizing function. The newly developed interpolation algorithm was used to reduce the sample size of the bi-planar fluoroscopic images which reduces radiation exposure. Experimental results illustrate the potential

success of the technique, but ultimately improvements in registration and validation methods are needed before becoming clinically viable.

Table of Contents

List of Figures

List of Tables

List of Abbreviations

2-D	Two-Dimensional
3-D	Three-Dimensional
ADL	Activities of Daily Living
AR	Axial Rotation
CC	Cranial-Caudal
CLAHE	Contrast-Limited Adaptive Histogram Equalization
COR	Center of Rotation
CT	X-Ray Computed Tomography
DAQ	Data Acquisition
DQHAM	Helical Axes of Motion with Dual-quaternions
DRR	Digitally Reconstructed Radiograph
FA	Foraminal Area
FD	Finite Difference
FE	Flexion-Extension
HAM	Helical Axes of Motion
HAM-r	Helical Axes of Motion - Rotation Component
HFZ	High Flexibility Zone
HSZ	High Stiffness Zone
LB	Lateral Bending
LBP	Low Back Pain
MDLT	Modified Direct Linear Transform
ME	Maximum Error
MRI	Magnetic Resonance Imaging
NI	National Instruments
NME	Normalized Maximum Error

NRMSE	Normalized Root Mean Squared Error
PA	Posterior-Anterior
RMSE	Root Mean Squared Error
ROM	Range of Motion
QHAM	Helical Axes of Motion with Quaternions
SCA	Spinal Canal Area
ScLERP	Screw Linear Interpolation
SLERP	Spherical Linear Interpolation
STL	STereoLithography ("Standard Tessellation Language")

Chapter 1

Introduction

Accurate assessment of patients' segmental spinal motion has remained an unresolved clinical problem primarily due to substantial measurement errors and lack of precision associated with the traditional methods of planar radiographic assessment coupled with manual measurements. However, the recent emergence of non-invasive 3-D kinematic assessment technologies have improved diagnostic capabilities.

1.1 Non-invasive In Vivo 3-D Motion Assessment

Currently, there are two leading non-invasive methods which combine bi-planar fluoroscopy with MRI or CT derived anatomic models to acquire in vivo 3-D spine kinematic data. One method computes vertebral silhouettes from the subject's spinal MRI model for registration to bi-fluoroscopic images acquired at discrete spinal postures to assess 3-D spinal motion [40, 43, 44, 56, 67, 68]. These authors have used this method to investigate lumbar segmental and facet joint motions in patients with disc degeneration. However, these researchers failed to create a continuous dataset since the bi-planar fluoroscopic data were only acquired at select discrete positions (neutral and end-ranges of motion), which lacks enough information to accurately interpret kinematics. Overall, the registration of vertebral anatomy is accurate, but the amount of kinematic information extracted is not enough to judge the quality of motion.

A second group of investigators acquire a continuous dataset using high-resolution CT scans in combination with bi-planar x-ray images taken using high-powered cardiac-cine angiography generators for 2-3 seconds at 30 frames per second [1–7]. This technique was used to measure 3-D motion in cervical spines of patients during dynamic flexion-extension and axial rotation activities. However, it is associated with increased radiation exposure and requires advanced imaging hardware not available in the clinical setting.

1.2 Interpolation of Discrete Kinematics

3-D spline functions can be used to recover a continuous kinematic dataset from the discrete positional data of vertebral bodies provided by registration of the 3-D models to bi-planar fluoroscopic images. Splines are continuous, smooth functions which are advantageous for characterizing motion and have therefore been prevalent in the 2-D kinematic analyses of the spine [48, 57]. Additionally, splines have the advantageous property of not being constrained by resolution and can have sub-pixel accuracy except at the boundary condition [48].

3-D wrist kinematic data have been interpolated using cubic splines [51]. When compared to linear interpolation, the cubic spline interpolation provides substantially more accurate predictions; however, an improved technique using the combination of cubic quaternion splines for interpolating the rotational component of motion and a cubic Hermite interpolator for location component of motion provides superior results to cubic spline interpolation [11]. Although accurate for the wrist, the usefulness of this newly developed method to interpolate 3-D spinal kinematic data has not been studied. Further, the methodology of the technique is not automated and may require manual adjustments for successful kinematic reconstruction.

1.3 Significance

In 2009, approximately 15% of Americans had neck pain and 39% had low back pain; females had significantly more pain than males [58]. American health related expenditures for back and neck pain for Americans where between $80.1 billion and $91.8 billion in 2005 [47]. Back pain is the second most common neurological ailment in the United States; only headaches are more common [12, 17, 36].

Current clinical standards for assessing in vivo spine motion are 2-D static single-plane or bi-plane X-rays, CT, and MRI obtained in full FE/LB/AR positions. Some pathologies, such as segmental instability, may not manifest in these extreme posture positions but rather in the midrange motion where the majority of ADL occur [53]. Further, the traditional radiographic images do not allow assessment of out-of-plane motions or other clinically relevant parameters such as motions occurring between the articular facet surfaces, a source of pain, or dynamic assessment of

foraminal and spinal canal spaces, which have implications to neurological symptoms. Therefore, the quantification of motion quality throughout the arc of motion will enhance the diagnostic capabilities. Regarding currently available non-invasive in vivo 3-D joint kinematic assessment techniques, these methods suffer from one or more limitations such as: (i) inability to acquire continuous, accurate 3-D kinematic data without subjecting the patients to excessive radiation, and (ii) the need for more advanced x-ray imaging technology than is likely available to clinicians and researchers at large.

The following research has laid the groundwork for developing a non-invasive method using clinically available technologies of CT imaging and digital fluoroscopy to accurately assess patients' 3-D in vivo spine kinematics. Such a method would significantly contribute to improving the care of patients with spinal disorders by enhancing diagnosis capabilities and providing improved means of assessing and monitoring outcomes following restorative surgeries that aim to restore physiologic quality of motion to the diseased segments.

1.4 Innovation

The contributions of this research include: (1) the development of a new 3-D kinematic interpolation algorithm, improving upon accuracy of previous techniques and allowing for a reduction in the necessary number of x-rays taken to acquire a continuous bi-planar kinematic dataset, (2) a robust, non-invasive in vivo kinematic assessment procedure utilizing tools that could be readily available to clinicians; and (3) a non-invasive method to acquire continuous 3-D kinematic data without excessive radiation; which in conjunction with the patient's 3-D anatomic model allow for a dynamic assessment of spine kinematic parameters and morphological interactions.

Chapter 2

Previous Work

Over the past several years, I have been a part of the development and refinement of an ex-vivo CT-based specimen-specific kinematic model to investigate the kinematics of lumbar and cervical spines including dynamic assessment of finite axes of rotation, facet joint motions, and spinal canal and foraminal areas. This modeling methodology was used to acquire the gold standard data needed to assess the accuracy of the proposed non-invasive techniques.

2.1 Gold Standard: Ex-Vivo CT-Based Specimen-Specific Kinematic Modeling

The following subsections outline a sampling of experiments which characterize both lumbar and cervical spinal kinematic parameters during flexion-extension motion. The details of the methodology and experimental setup are described in Section 5.2.5.

2.1.1 Dynamic Assessment of Spinal Canal and Foraminal Area [33, 34]

Degenerative changes of the cervical and lumbar spine in the form of bone spurs and disc space narrowing affect both the area available for the nerve roots as well as the space available for the spinal cord. Additionally, the spinal canal and foraminal areas are greatly affected by the posture of the spine. Traditional techniques to evaluate the foraminal dimension have used direct measurement by caliper and blunt probe and measurement using CT scans in static postures [22]. These studies assessed the neural foramen and spinal canal areas continuously through the ROM of intact spine specimens undergoing FE ROM testing.

Methods: Cadaveric spines (C3-T1, 9; L1-S1, 6) were evaluated using CT-Based specimen-specific kinematic modeling. As a result, motion of any anatomical landmark could be assessed in response to loads applied during flexibility testing. Angular motion, spinal canal area as well as the foraminal area of the C5-C6 as well as foraminal area and height of the L2-L3 and L3-L4 motion segment were calculated (Fig. 2.1). The details of the computation scheme for kinematic

parameters are presented in Section 4.2.2.

Results: The foraminal areas for all specimens increased in flexion and decreased in extension with regression analysis showing a significant correlation between normalized foraminal area and angular motion ($R^2 \leq 0.87$, $p < 0.05$) as well as percent change in cervical spinal canal area and angular motion ($R^2 = 0.89$, $p < 0.05$). Spinal canal area was not evaluated for lumbar spine, but the applied concept is illustrated in Fig. 2.2.

2.1.2 Dynamic Assessment of Facet Kinematics [30–32]

The goal of this study was to assess the facet engagement in intact cervical spine specimens undergoing motions in FE and AR using the discussed specimen-specific CT model.

Methods: Nine cadaveric spines were used and evaluated using the 3-D specimen-specific anatomical model. Using the kinematic data and facet morphology from the CT model, facet overlap area was calculated throughout the ROM in FE and AR. Overlap calculations were performed in the plane of the superior facet surface of the inferior vertebrae of each joint (Fig. 2.3). Facet planes were determined from a least squares fit to points on the facet perimeter.

Results: In C6=C7 AR the overlap area on the contralateral facet decreased relative to neutral posture, whereas the ipsilateral facet area did not change ($p < 0.05$). The total FE facet overlap area was similar for both C5-C6 and C6-C7 ($p > 0.05$). At both levels flexion motion significantly reduced facet overlap area relative to the neutral posture ($p < 0.05$). Extension motion had a smaller effect on facet overlap area compared to neutral at both segmental levels.

2.1.3 Dynamic Assessment of the Facets Role in Governing Flexion-Extension Motion

Cervical facets are known to contribute significantly to the biomechanics of the cervical spine. The purpose of this study was to investigate the correlation between facet morphology and FE motion patterns.

Methods: Seven fresh frozen human cadaveric cervical (C3-T1) specimens were procured and analyzed. COR of each motion segment was evaluated relative to a local Cartesian system defined on the inferior vertebrae for FE motion (Fig. 2.4).

Results: Facet inclination angle with respect to vertebral level had no discernable trend ($p = 0.407$). The facet midpoint location statistically increased in both the PA and CC directions while descending down the cervical spine (p=0.037 and $p < 0.001$ respectively). Segment level did not impact the PA position of COR ($R^2 < 0.01$, $p = 0.935$), but was shown to be inversely proportional to COR in the CC direction ($p < 0.001$). As the midpoint and superior facet point trended in the cranial direction, COR z-position did as well ($p < 0.001$ and $p < 0.001$ respectively). Finally, as the facet midpoint moved posteriorly, COR moved in the cranial direction ($p = 0.001$).

2.2 Figures

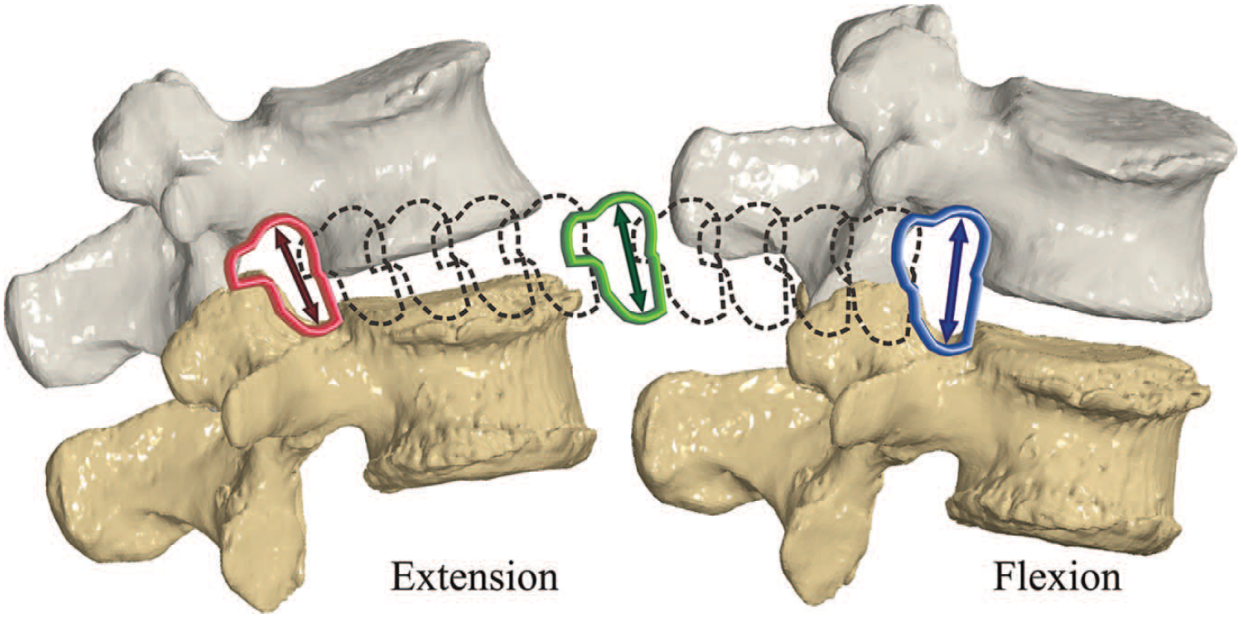

Figure 2.1: Dynamic assessment of foraminal area and height during extension-to-flexion motion using the 3-D CT-based specimen-specific model. Foraminal area and height are smallest in extension and largest in flexion. Contours are traces of neuroforaminal area and arrows show the foraminal height

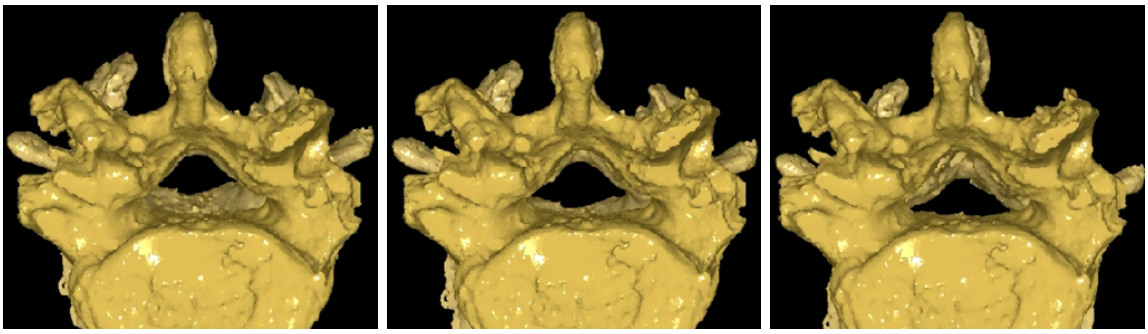

(a) (b) (c)

Figure 2.2: Dynamic assessment of spinal canal stenosis in an L4-L5 degenerative spondylolisthesis specimen using the specimen-specific model. L4 flexing on L5 viewed from caudal to cranial perspective. (a) extension, (b) neutral, (c) flexion. The anterior slip of L4 on L5 and narrowing of the spinal canal are clearly visible.

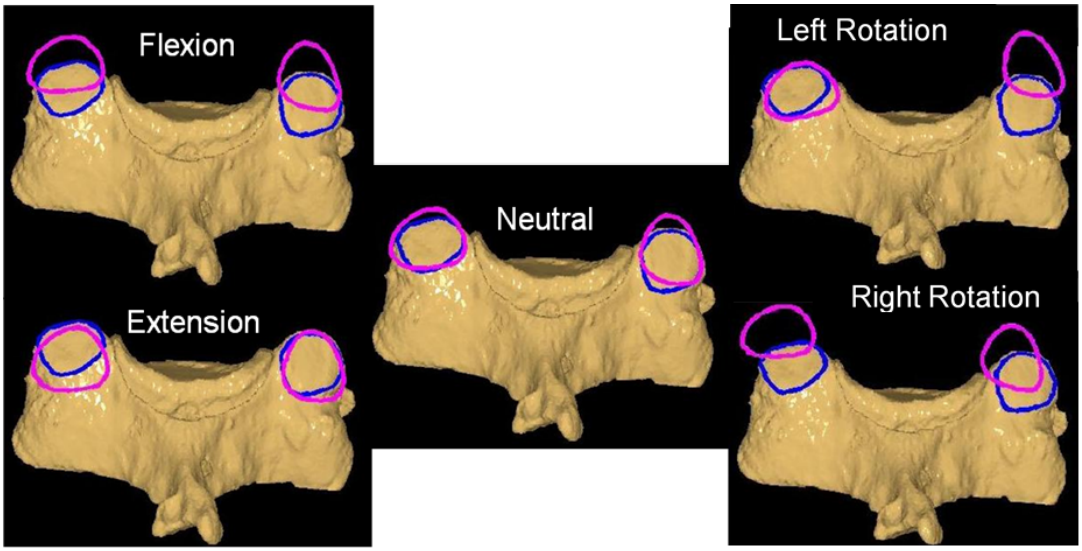

Figure 2.3: Overlap area of C5-C6 facet surfaces.

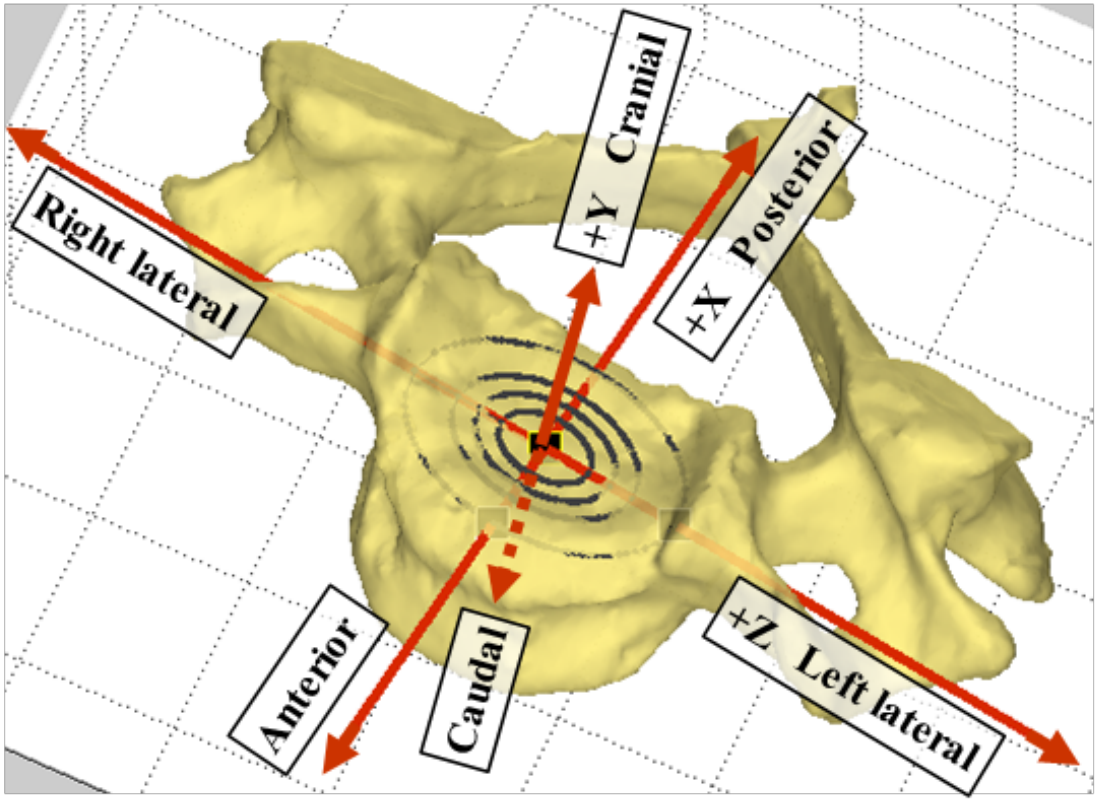

Figure 2.4: C4-C5 local coordinate system located on the center of C5 superior endplate.

Chapter 3

Interpolation of Three Dimensional Kinematics with Dual-quaternions[1]

3.1 Introduction

Bi-planar x-ray registration is a recent 3-D dynamic assessment technique which evaluates patient-specific kinematics non-invasively. This technique utilizes x-ray images taken simultaneously from two known relative locations to track the orientation and position of rigid bodies previously reconstructed from a 3-D anatomical computed tomography (CT) scan.

To accomplish this some authors have used high frame rate videofluoroscopy which provides good kinematic description, but has high radiation exposure [41]. Alternatively, using low frame rate digital fluoroscopy, a smaller number of x-rays can be taken during a continuous range of motion providing less kinematic data with lower radiation exposure. In order to produce a high quality kinematic dataset with reduced radiation exposure, low frame rate x-ray data can be interpolated.

Coburn and Crisco (2005) illustrate how interpolation methods can be used to produce high quality kinematic data with reduced radiation exposure [11]. They used cubic splines to interpolate their motion descriptor, a variation of the helical axis of motion (HAM) which contains both a rotation and translation component, but not without limitation. The two components must be interpolated separately, forcing the authors to make assumptions about their synchronization and resulting in loss of coordinate invariance due to dependence on the arbitrary reference frame in which the origin in determined. Further, the authors attempt to adjust for non-uniform x-ray intervals based upon tangent, continuity, and bias controls (TCB-spline; Kochanek and Bartels, [39]) and average rotation between frames, but provide no algorithm for determining TCB values.

The purpose of this study was to further develop existing 3-D kinematic interpolation techniques such that its use for bi-planar x-ray registration minimizes sampling size while maintaining

[1]This article was published in Journal of Biomechanics: Jeremy E. Goodsitt, Robert M. Havey, Saeed Khayatzadeh, Leonard I. Voronov, and Avinash G. Patwardhan. Interpolation of three dimensional kinematics with dual-quaternions. Journal of Biomechanics, 2016. http://dx.doi.org/10.1016/j.jbiomech.2016.10.028 and reprinted with permission from Elsevier.

a high degree of accuracy in representing the true motion. Improvements are made by achieving the following goals: (i) choosing an appropriate motion descriptor for interpolation, (ii) improving autonomous adjustment of control point tangents for non-uniformly spaced x-rays and (iii) developing an algorithm to minimize the number of interpolant control points while maintaining a high degree of accuracy.

3.2 Methods

Extrapolated from previous techniques, a new approach for interpolating 3-D kinematics is described. Using a specimen specific kinematic analysis technique (Fig. 3.1a-b)(Havey et al., [34]), vertebral flexion-extension motion data from a cadaveric lumbar spine were collected at a high sampling rate. Motion data were then down-sampled, interpolated, and compared to the original dataset. Accuracies between the sets of motion descriptors and interpolation methods (Table 3.1) were also evaluated (Fig. 3.1c).

3.2.1 Motion Descriptors and Interpolators

The most well-known rigid body motion descriptor is the coordinate transformation matrix, although it does not produce rational motions when using standard interpolation techniques. Thus, new techniques such as the composite representation of the HAM (QHAM; Coburn and Crisco, [11]) or the homogenous description by dual-quaternions (Ge and Ravani, [24]) are used. HAM are coordinate invariant, unlike joint coordinate systems (Euler angles) which require anatomical relationships (Blankevoort et al., [8]), therefore simplifying interpolation; however in this study, the HAM appears similar to Euler decomposition due to the primarily planar motion in flexion-extension. The physical interpretation of HAM becomes more difficult when movement occurs outside of one of the cardinal planes. Provided that the axis and location components of HAM are described in reference to an anatomical coordinate system, HAM can first be converted into direction cosine matrix and subsequently into its Euler decomposition for clinically relevant values (Blankevoort et al., [8]; Kenwright, [37]). The subsequent section discusses the dual-quaternion interpolator implementation in detail, however refer to Gouasmi [26] for a dual-quaternion introduction and Coburn and Crisco [11], Dam et al. [15], and Hamilton [27] for quaternion implementation.

Dual-quaternion Interpolation (DQHAM)

Similarities between quaternions and dual-quaternions allow one to generalize quaternion interpolation algorithms for dual-quaternions. Screw linear interpolation (ScLERP) is the generalized form of SLERP for dual-quaternions:

$$\text{ScLERP}\left(\hat{\mathbf{p}}, \hat{\mathbf{q}}; t\right) = \hat{\mathbf{p}}\left(\hat{\mathbf{p}}^{*}\hat{\mathbf{q}}\right)^{t} \tag{3.1}$$

Analogous to quaternions, dual-quaternions are also antipodal ($\hat{\mathbf{q}} = -\hat{\mathbf{q}}$), hence it is important to specify the correct orientation of $\hat{\mathbf{q}}$ relative to $\hat{\mathbf{p}}$ for ScLERP to take the shortest path. Ge and Ravani describe how Shoemaker's cubic quaternion spline, utilized by QHAM, can also be applied to dual-quaternions via ScLERP, forming the basis for DQHAM [24].

For DQHAM to account for non-uniform data, a new, automated method derived from the Taylor series was devised to properly weight the effect each dual-quaternion has on the control point tangents, $\hat{\mathbf{a}}_\mathbf{i}$ and $\hat{\mathbf{b}}_\mathbf{i}$ with the correction factor C_s. For ease of comprehension, the tangent derivations are first described in the Cartesian domain and subsequently for dual-quaternions:

$$\begin{aligned} r_{i+} &= r_i + \frac{(r_{i+1} - r_i) + C_s(r_i - r_{i-1})}{2} \\ r_{i-} &= r_i + \frac{\frac{1}{C_s}(r_i - r_{i+1}) + (r_{i-1} - r_i)}{2} \end{aligned} \tag{3.2}$$

$$\begin{aligned} \hat{\mathbf{a}}_\mathbf{i} &= \text{Bisect}\left(\text{ScLERP}\left(\hat{\mathbf{q}}_{\mathbf{i-1}}, \text{Double}\left(\hat{\mathbf{q}}_{\mathbf{i-1}}, \hat{\mathbf{q}}_\mathbf{i}\right), 0.5 + \frac{C_s\left(a\right)}{2}\right), \hat{\mathbf{q}}_{\mathbf{i+1}}\right) \\ \hat{\mathbf{b}}_\mathbf{i} &= \text{Bisect}\left(\text{ScLERP}\left(\hat{\mathbf{q}}_{\mathbf{i+1}}, \text{Double}\left(\hat{\mathbf{q}}_{\mathbf{i+1}}, \hat{\mathbf{q}}_\mathbf{i}\right), 0.5 + \frac{1}{2C_s\left(b\right)}\right), \hat{\mathbf{q}}_{\mathbf{i-1}}\right) \\ \hat{\mathbf{b}}_\mathbf{i} &= \text{ScLERP}\left(\hat{\mathbf{a}}_\mathbf{i}, \text{Double}\left(\hat{\mathbf{a}}_\mathbf{i}, \hat{\mathbf{q}}_\mathbf{i}\right), 0.5 + \frac{1}{2C_s\left(b\right)}\right) \end{aligned} \tag{3.3}$$

Similar to QHAM, equation 3.3 only functions for the interior points of the spline. At the extrema, finite differencing (FD) must be applied to create an additional point to satisfy its constraints. Improving upon QHAM's two-point FD, this study used a weighted three-point FD which also accounts for non-uniform sampling with a temporal correction factor C_{FD}.

$$hf'\left(x\right) = \frac{c^2 f\left(x+h\right) - f\left(x+ch\right) - \left(c^2-1\right) f\left(x\right)}{c\left(c-1\right)} \tag{3.4}$$

$$\hat{\mathbf{q}}_{\mathbf{-1}} = \hat{\mathbf{q}}_{\mathbf{1}}\text{ScLERP}\left(\hat{\mathbf{I}}, \left(\text{ScLERP}\left(\hat{\mathbf{I}}, \hat{\mathbf{q}}_{\mathbf{3}}, c^2\right)\hat{\mathbf{q}}_{\mathbf{2}}^{*}\text{ScLERP}\left(\hat{\mathbf{I}}, \hat{\mathbf{q}}_{\mathbf{1}}, 1-c^2\right)\right), \frac{1}{c(c-1)}\right)$$
$$\hat{\mathbf{q}}_{\mathbf{m+1}} = \hat{\mathbf{q}}_{\mathbf{m}}\text{ScLERP}\left(\hat{\mathbf{I}}, \left(\text{ScLERP}\left(\hat{\mathbf{I}}, \hat{\mathbf{q}}_{\mathbf{m-2}}, c^2\right)\hat{\mathbf{q}}_{\mathbf{m-1}}^{*}\text{ScLERP}\left(\hat{\mathbf{I}}, \hat{\mathbf{q}}_{\mathbf{m}}, 1-c^2\right)\right), \frac{1}{c(c-1)}\right) \quad (3.5)$$
$$C_{FD-} = \frac{t(3)-t(2)}{t(2)-t(1)}, C_{FD+} = \frac{t(m)-t(m-1)}{t(m-1)-t(m-2)}$$

where $\hat{\mathbf{I}}$ is the identity dual-quaternion, c is the step size scaling factor, t is time, and m represents the sample size.

Tangent Correction Factors

Three correction factor methods will be assessed for all motion descriptors where applicable: (1) correction based upon the average motion of the original dataset (Avg; Coburn and Crisco, [11]), (2) correction based upon relative motion between the interpolated and adjacent segments (Local), and (3) temporal adjustment (Time). Let S represent the arc length, θ_i the HAM angle, and $C_s(a)$ and $C_s(b)$ are the correction factors for $\mathbf{a_i}$ or $\hat{\mathbf{a}}_\mathbf{i}$ and $\mathbf{b_i}$ or $\hat{\mathbf{b}}_\mathbf{i}$ respectively:

$$\begin{aligned} \text{S}_{ideal} &= \frac{\sum_i \theta_i}{\sum_i 1_i} \\ C_s(a) = C_s(b) &= \frac{\text{S}_{actual}}{\text{S}_{ideal}} \end{aligned} \quad (3.6)$$

$$C_s(a) = \frac{\theta_i}{\theta_{i-1}}, C_s(b) = \frac{\theta_i}{\theta_{i+1}} \quad (3.7)$$

$$C_s(a) = \frac{t_{i+1}-t_i}{t_i-t_{i-1}}, C_s(b) = \frac{t_{i+1}-t_i}{t_{i+2}-t_{i+1}} \quad (3.8)$$

Specimen and Experimental Setup

Motion of four lumbar vertebrae (L2-L5) from a cadaveric spine (L1-S1) (56yo, Male) were captured using an optoelectronic motion measurement system (Model 3020, Optotrak, Northern Digital, Waterloo, ON, Canada) via six infrared targets attached rigidly to each vertebrae while FE moments were applied to the L1 vertebrae as presented by Havey et al. [34]. Additionally, four radiopaque fiducial markers were implanted in each vertebrae for anatomical registration between the infrared targets and vertebral anatomy (Havey et al., [34]).

Data Collection and Sampling

Flexion-extension (8 Nm, -5.5 Nm respectively; 0.135 Nm/sec) motion data were collected at 30 ', clipped to one single extension-to-flexion motion (Fig. 3.2a), and down-sampled to represent discrete images simulating in vivo data collection. Vertebral rigid body locations were then calculated from their respective original and interpolated kinematic datasets. The motion descriptor, tangent correction factor, and sample spacing were variables in determining the ideal interpolation algorithm. Two general sampling techniques, moment and angle, and an optimized sampling method specifically for the spine were used to decimate data (Fig. 3.2b). Moment and angular sampling were broken in two categories: (1) equally distributed sampling, and (2) flexible sampling where sampling points were equally distributed on either side of a specific area of interest (neutral posture for this study). Sample size for both moment and angular methods varied between 3 and 20 (0.12% and 0.80% normalized rate respectively). Optimized sampling methods adjusted sample location based upon known features of spinal motion, the high flexibility zone (HFZ) and high stiffness zone (HSZ) (Fielding et al., [20]; Stolworthy et al., [64]). Optimized control point locations were equally spaced between a percentage of flexion and extension motion. For example, the sampling 1/3E-2/3F indicates that all sampling points except for the extrema were equally spaced between one-third of the maximum extension angle and two-thirds the maximum flexion angle (Fig. 3.2b). Optimized sampling tests were sample size limited between 3 and 9 (0.12% and 0.36% normalized rate respectively).

Accuracy Comparison

Driven by both the original and interpolated datasets, the 3-D position of each vertebra's fiducial markers were used for comparison. Interpolated points were synchronized with the original dataset before analysis. Root mean square error (RMSE) and maximum error were normalized to the total distance traveled of the original data (NRMSE, NME) and used to evaluate overall accuracy of each interpolated point. L2-L5 vertebrae total distance traveled were 53.30, 33.48, 17.95, and 7.24 mm respectively. Finally, NRMSE was applied to average the error descriptors of the four markers and reported.

Bonferroni correction, $p\mathrm{N} < \alpha$, was applied individually to each N-comparison two-tailed t-tests.

3.3 Results

Overall, DQHAM methods were superior to QHAM in reconstructing the original dataset and only QHam-Avg was more accurate than ScLERP for all sampling techniques. DQHAM-Time had the best results when comparing sample sizes above nine (NME: 2.96%, NRMSE: 0.93%; Fig. 3.3a-b). Excluding optimized sampling techniques, equal angles sampling was statistically more accurate when the sample size was more than seven (NME: $p < 0.01$ and NRMSE $p < 0.05$, N = 3). Increases in accuracy were marginal for all methods by sample size 20.

Due to the large number of combinations, the best non-optimized sampling method with highest accuracy (equal angle) is used to discuss the effectiveness of each interpolator. A comparison of interpolation error for equal angles sampling was made (Table 3.2). Equal angles NME and NRMSE plots show a visual divide between QHam and other motion descriptors (NME: $p < 0.01$, NRMSE: $p < 0.05$, N = 6; Fig. 3.4). Regardless, all interpolation combinations behaved similarly before the inflection point; after the inflection point DQHAM-Time had reduced error compared to other techniques. Statistically, DQHAM-Time had lower NME and NRMSE for sample sizes more than eight (Fig. 3.4b-c).

The trend between accuracy and total distance traveled was evaluated for all equal angle combinations (Fig. 3.4d-e). The exponents of the power regression models were not equal to 0 or ± 1, indicating that RMSE was not a constant. The regressions were similar for all combinations of NME vs total distance. However, DQHAM-Time's initial value was 20% lower than the next closest combination. Additionally, DQHAM-Time NRMSE had an initial value 34% lower and its regression decreased more rapidly than other combinations. Equating feature based sampling techniques to the best non-optimized sampling technique, only optimized sampling methods, 2/3E-5/6F and 3/5E-5/6F combined with DQHAM-Time, presented higher accuracy at lower sampling rates (Fig. 3.5). Accuracy for these two combinations achieved the same asymptotic accuracy as the optimal equal angles method with a sample size of seven.

3.4 Discussion

The aim of this study was to improve upon existing interpolation techniques such that its use for bi-planar fluoroscopy would produce an optimized balance between x-ray sample size and kinematic reconstruction error. As a result, many interpolation and sampling techniques were evaluated and compared.

3.4.1 Improvements

Due to the likeness between quaternions and dual-quaternions, QHAM was able to be seamlessly applied to dual-quaternions creating DQHAM and allowing for the simultaneous solution to rotation and translation as well as maintaining reference frame invariance (Ge and Ravani, [24]). Moreover, DQHAM introduced programmatically determined weights to the control point tangent calculation to account for non-uniform sampling distributions providing a significant reduction in error compared to QHAM without its TCB inputs which would have been computed manually, post-hoc. Additional improvements were made at the extrema to the tangent calculation with a weighted three-point FD ($p < 0.01$, N = 2); used by both QHAM and DQHAM, but not applicable to the linear interpolation scheme ScLERP.

3.4.2 In Vivo Application

In vivo analysis requires a delicate balance between accuracy and radiation exposure. Interpolation error was discovered to follow a power regression model, defining a point of diminishing returns regarding sample size. Less successful sampling techniques likely suffered from large sampling gaps surrounding areas of higher velocity or the nonlinear relationship between bending moments and vertebral motion. In contrast, feature based sampling techniques were able to optimize the sample size to accuracy equilibrium by concentrating samples around the HFZ where higher angular velocity occurs, emphasizing the importance of control point placement. Unfortunately, the results for feature based optimization are limited and may not represent general success of the technique. Therefore, using equal angles is currently recommended due to its ease and accuracy.

The combination of DQHAM-Time with equal angles sampling provided the best results (NME: <2%, NRMSE: 1%), reaching its accuracy plateau at a sample size of nine and demonstrated

its scalability. However, when interpolating a more intricate motion pattern, error may increase depending on sample size and sample locations as illustrated by the feature based optimization. In addition, in vivo kinematic reconstruction also introduces sampling complications. For instance, when sampling relative to angular motion, one only has access to the gross motion of the patient. Hence, its success is dependent on the rigid bodies being tracked mimicking the gross motion of the subject; in cases where multiple rigid bodies are tracked, all are assumed to have similar angular motion responses.

3.4.3 Limitations and Future Work

More analysis is required to evaluate the assumption that the interpolation parameter t, varies linearly with time and does not require separate variables for orientation and translation. Further, motion was generally planar and had limited translation, hence success for other joints which may have more complicated motions requires evaluation.

Future work will assess the effects on kinematic parameters such as velocity and acceleration, the instantaneous axis of rotation, and morphological interactions which have unknown interpolation sensitivity.

3.5 Conclusion

This studies goal was to develop a 3-D interpolation method to accurately define kinematic motion while minimizing the data sample size. Using the proposed method, reducing the range of motion sample size to nine postures does not affect accuracy in this ex vivo model. The ability of multiple interpolation and sampling methods to reconstruct 3-D rigid body kinematics were compared. Dual-quaternions with time derived control point tangents and equal angle sampling provides robust accuracy with a low sample size effectively minimizing radiation exposure.

3.6 Acknowledgments

Financial support was given by the Small Projects in Rehabilitation Research (SPiRE) Award from the VA Rehabilitation R&D.

3.6.1 Conflicts of Interest

There were no conflicts of interest associated with the presented work by any of its authors.

3.7 Figures

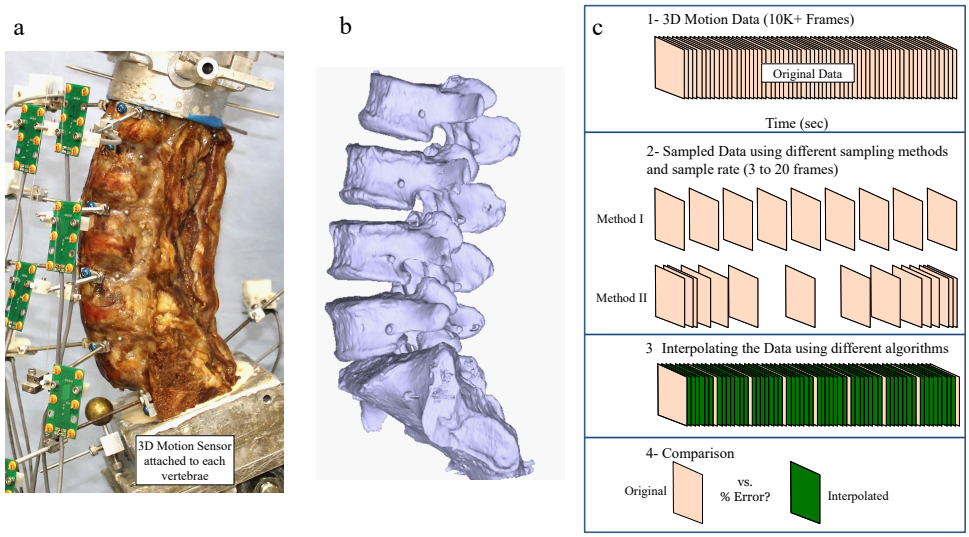

Figure 3.1: a) Lumbar specimen testing setup. b) 3-D reconstruction of the lumbar specimen. c) Demonstration of motion data decimation and interpolation. The method goal is to find an algorithm and sampling method which gives the least error at the minimum sample rate.

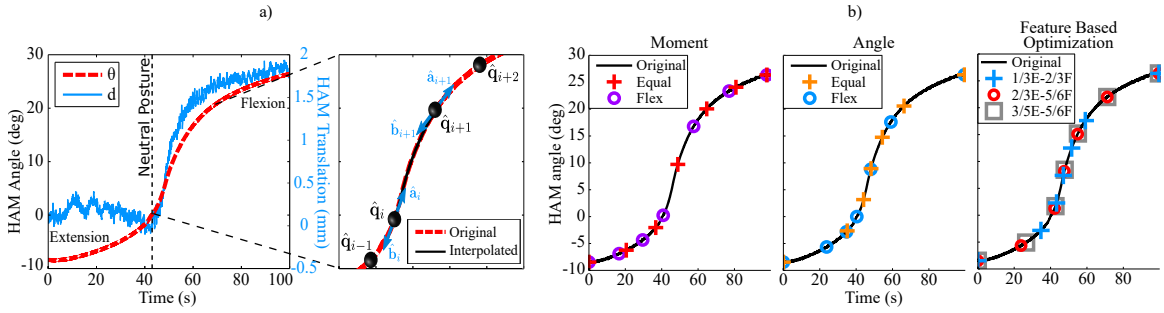

Figure 3.2: a) L2 HAM translation (d) and orientation (θ) throughout the test and an illustration of the dual-quaternion spline curve and the control points ($\hat{\mathbf{q}}_\mathbf{i}$) with their respective tangents $\hat{\mathbf{a}}_\mathbf{i}$, $\hat{\mathbf{b}}_\mathbf{i}$) used for curve reconstruction. Beginning in extension, L2 reaches neutral posture at 43s and finishes in flexion. b) Examples of moment, angle, and feature-based optimized sampling for the L2 vertebrae (interpolation N = 7).

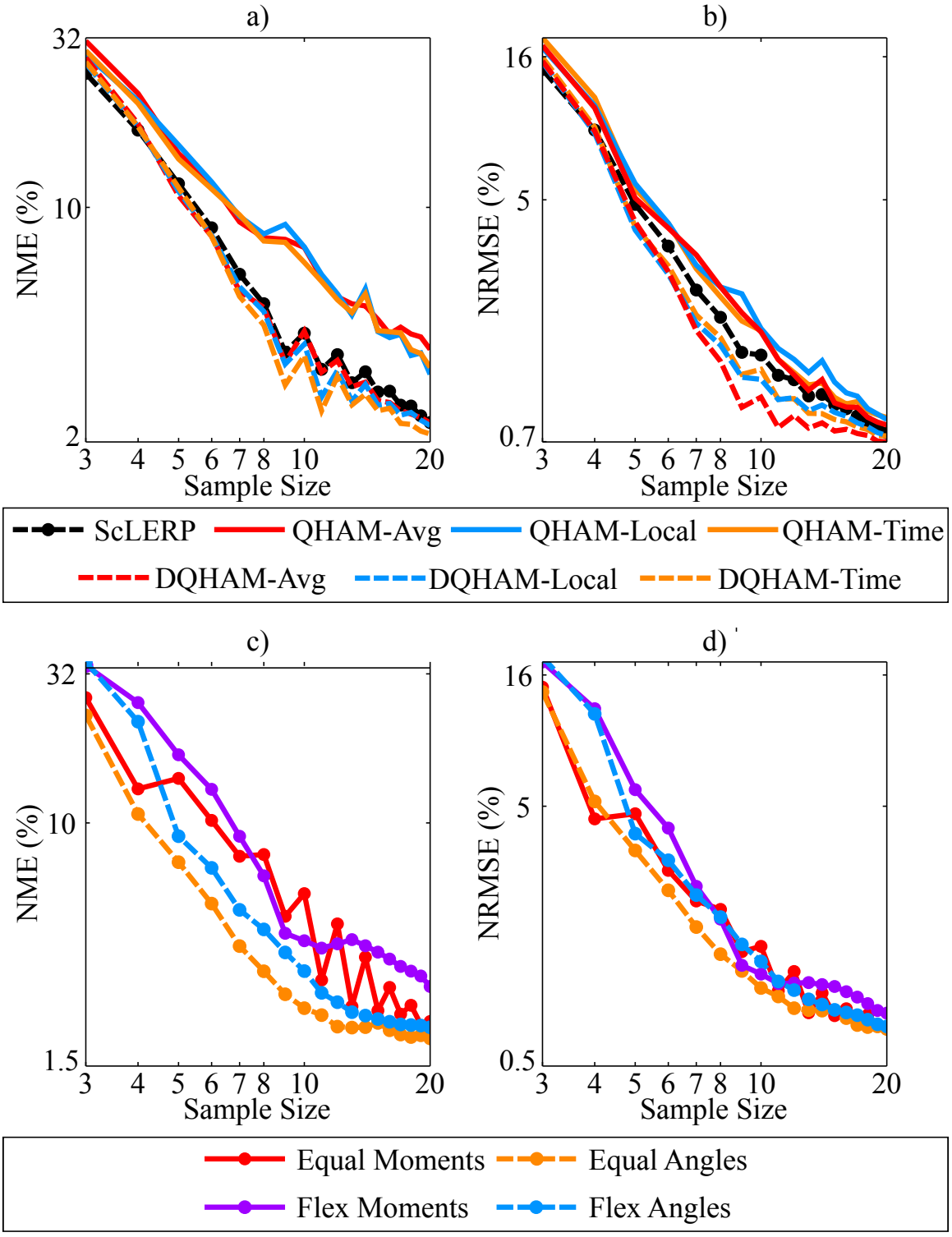

Figure 3.3: Accuracy for each interpolation technique averaging the sampling methods and vertebrae for (a) NME and (b) NRMSE as well as accuracy for each non-optimized sampling method averaging the interpolation techniques and vertebrae for (c) NME and (d) NRMSE. Both NME ($R^2 = 0.98$, $R^2 = 0.96$) and NRMSE ($R^2 = 0.93$, $R^2 = 0.93$) demonstrated a strong correlation to a power regression model for interpolation technique and sampling technique respectively.

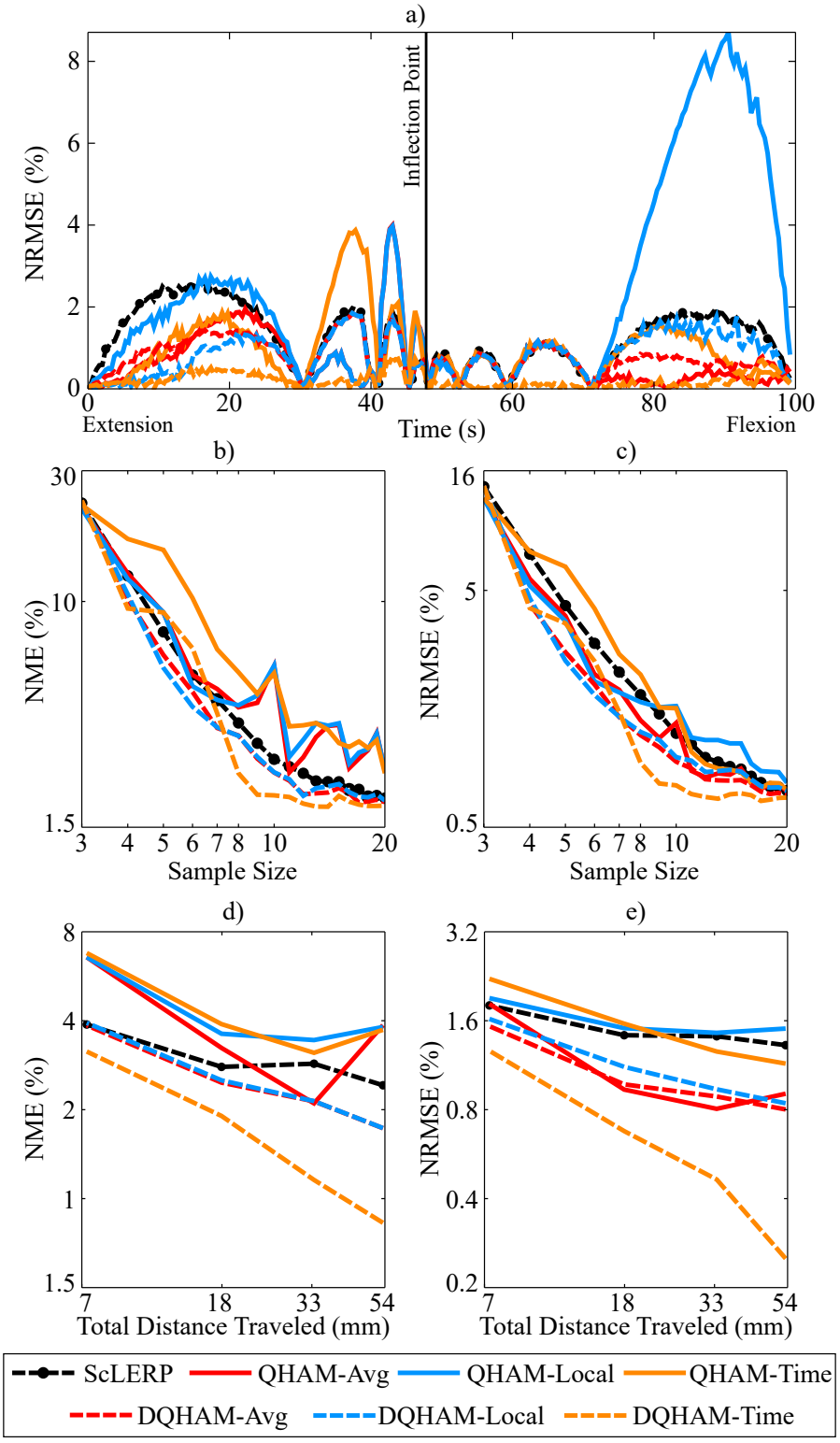

Figure 3.4: Illustration of the equal angles sampling reconstruction methods using all interpolation algorithms: a) extension-to-flexion of the L2 vertebra, NRMSE of equal angles interpolation error (N = 9), b) NME vs sample size, c) NRMSE vs sample size, d) NME for constant sample size (N=9), and e) NRMSE for constant sample size (N = 9). As the motion of the rigid body increases interpolation error decreases relative to the total distance traveled.

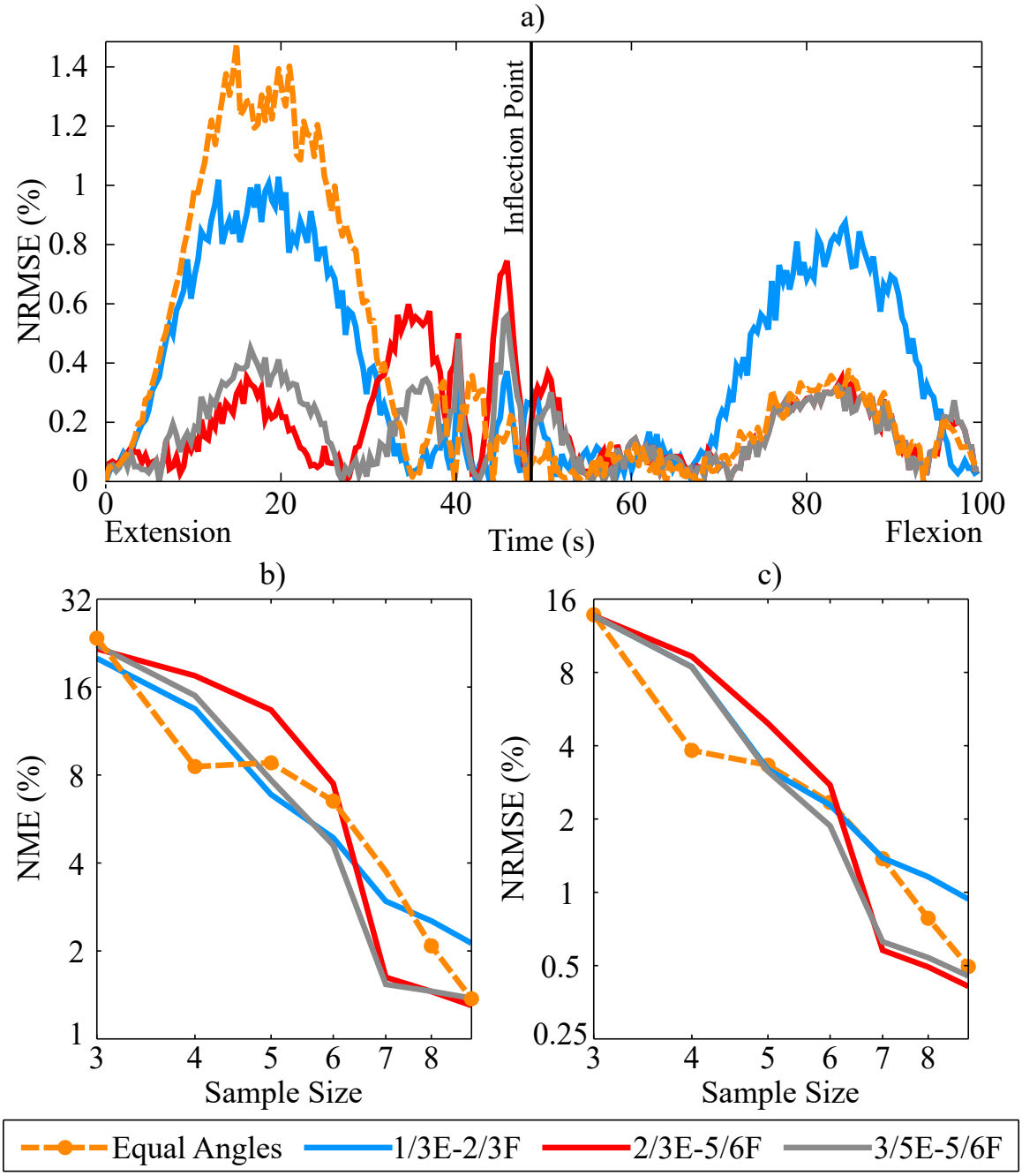

Figure 3.5: Comparing optimized reconstruction methods vs equal angles sampling: a) extension-to-flexion of the L2 vertebra, NRMSE of optimal feature based sampling and equal angles DQHAM-Time distance error with a sample size of seven, b) NME vs sample size, and c) NRMSE vs sample size. Due to normalized error increasing exponentially as the total distance approaches zero, L5 was removed to avoid misrepresentation of the results in b) and c).

Table 3.1: Overview of the study's interpolation algorithms, sampling techniques and sizes, accuracy results, and figure/table references.

Interpolation Requirements	Algorithm Options		Optimum Reconstruction Algorithm			Referenced Comparison Figure /Table
Reconstruction Algorithm	ScLERP					Figure 3, 5-8 Table 2
	QHam DQHAM	Tangent Sub Options: **Avg** **2-Point FD** **Local** **3-Point FD** **Time**	DQHAM	**Time**	**3-Point FD**	
Sampling Method	Moment	**Spacing Sub Options:** **Equal** **Flexible**	Angle	**Equal Spacing**		Figure 2, 4, 7
	Angle	**Equal** **Flexible**				
	Stiffness Zone	Spacing Sub Options: **1/3E-2/3F** **2/3E-5/6F** **3/5E-5/6F**	Stiffness Zone	**3/5E-5/6F**		
Sample Size	3 to 20 (Asymptotic Solution)		Larger increases accuracy Accuracy plateaus 9 samples			Figure 3-7

Table 3.2: Interpolation NME and NRMSE for equal angles sampling (N = 9). Average error for each vertebrae and for each interpolation method are shown with DQ-Time providing the best results.

		ScLERP	QHam-Avg	QHam-Local	QHam-Time	DQ-Avg	DQ-Local	DQ-Time	Average	Distance Traveled (mm)
NME	L2	2.42%	3.86%	3.81%	3.73%	1.73%	1.73%	0.83%	2.82%	53.3
	L3	2.86%	2.10%	3.44%	3.12%	2.14%	2.14%	1.16%	2.52%	33.48
	L4	2.79%	3.24%	3.61%	3.90%	2.47%	2.51%	1.90%	2.99%	17.95
	L5	3.88%	6.56%	6.56%	6.78%	3.86%	3.93%	3.15%	5.17%	7.24
	Average	3.04%	4.27%	4.54%	4.60%	2.67%	2.71%	1.97%	3.54%	32.93
NRMSE	L2	1.32%	0.91%	1.50%	1.15%	0.80%	0.84%	0.25%	1.04%	53.3
	L3	1.42%	0.81%	1.46%	1.26%	0.89%	0.94%	0.46%	1.09%	33.48
	L4	1.43%	0.94%	1.51%	1.56%	0.97%	1.12%	0.68%	1.21%	17.95
	L5	1.80%	1.82%	1.91%	2.22%	1.53%	1.62%	1.27%	1.76%	7.24
	Average	1.50%	1.19%	1.61%	1.60%	1.09%	1.17%	0.76%	1.31%	32.93

Chapter 4

Interpolation of Spine Kinematic Parameters with Dual-quaternions

4.1 Introduction

Narrowing of the central or lateral nerve root canals as well as spinal instability resulting from intervertebral disc degeneration is well documented for its role in symptomatic radicular pain [49]. Although, degenerative lumbar disorders occur in many asymptomatic patients as well [42], illustrating the need for thorough diagnostic techniques to distinguish between symptomatic and asymptomatic cases. Cross-sectional magnetic resonance imaging (MRI) of the lumbar spine is a common diagnostic technique for patients with low back pain (LBP), but is limited to addressing one posture [34], may inaccurately describe foraminal or spinal canal stenosis due to out-of-plane measurements [23], and does not address subject-specific kinematics which have been shown to impact canal narrowing [50]. While lumbar nerve root compression has been shown to be caused by morphological factors, the interaction between morphology and subject-specific kinematics has only recently been addressed [34, 50].

2D-3-D bi-planar registration has emerged as a successful non-invasive in vivo 3-D patient-specific technique to evaluate spine kinematics which inherently addresses some concerns of static MRI diagnostics. However, bi-planar registration is limited by radiation dosage resulting from both the bi-planar x-ray imaging and the 3-D model used for registration, typically obtained using computed tomography (CT). Using existing patient-specific 2D-3-D technologies, a choice must be made regarding the number of x-ray images to take through the subject's motion. A small number of x-rays may provide an incomplete description of spinal kinematics, but with lower radiation exposure [40, 43, 44, 56, 67, 68] or, videofluoroscopy can capture the entire motion dataset [1–7] but at the expense of higher radiation exposure from a larger x-ray sampling size. A recent study has illustrated interpolation techniques which can be used to recover a full kinematic dataset from bi-planar registration methods with a low sample size. These method have produced limited

reconstruction error for positional data [11, 25], but evaluation of the interpolation methods on complex kinematic parameters has been nonexistent.

The aim of this study was to evaluate the sensitivity of reconstruction error for complex kinematic parameters using 2D-3-D bi-planar reconstruction methods and assess the viability for in vivo evaluation. Three kinematic parameters are discussed: (i) the helical axes of motion (HAM) [16], (ii) foraminal area (FA) [34], and (iii) spinal canal area (SCA). Consequently, a new method is described for measuring in vivo SCA and a preliminary dataset illustrating the effect of extension-to-flexion motion on the kinematic parameter within the lumbar spine is provided.

4.2 Methods

Data and motion interpolation techniques [25] are applied to a kinematic dataset in order to evaluate the accuracy of calculating complex kinematic parameters which are influenced by adjacent vertebral bodies. Cadaveric lumbar vertebral flexion-extension lumbar motion data were collected at a high frequency using a specimen-specific kinematic analysis technique (Fig. 4.1a-b) [34]. Morphologically derived parameters were first digitized before being driven by the anatomy's motion using custom MATLAB (Mathworks Inc., Natic, MA, USA) scripts. In vivo sampling was simulated by decimating the original motion data. Interpolation techniques (Table 4.1) were applied to the decimated dataset, kinematic parameters were calculated and compared to the kinematic parameters resulting from the original motion data (Fig. 4.1c).

4.2.1 Specimen and Experimental Setup

One intact fresh frozen human cadaveric lumbar spine (L1-S1; 56yo male) was kinematically tracked while undergoing flexion-extension motion. Following the procedure outlined by Havey et al. [33,34], the specimen was screened for pathologies which could significantly affect spine biomechanics. The paraspinal muscles were removed while preserving intervertebral discs, ligaments, and posterior structures. Four radiopaque fiducial markers (1.6 mm radius) were rigidly fixed to each vertebrae (L2-S1). Prior to kinematic testing, a CT scan (LightSpeed VPT, GE Medical Systems; $0.293 \times 0.293 \times 0.625$ mm) of the specimen was acquired from which a 3-D specimen-specific anatomical model was reconstructed.

As described by Havey et al. [33, 34], morphological features (foramen and spinal canal) were digitized on the anatomical model. These features were then driven by 3-D motion measurement data (Optotrak Certus, Northern Digital, Waterloo, Ontario, Canada) collected from custom 3-D motion measurement targets rigidly attached to each vertebrae. This was done by using the geometrical relationships between each vertebral anatomical model and its motion measurement target located in the Optotrak coordinate system. The fiducial markers attached to each vertebral body were originally captured in the CT-Scan and later located in the Optotrak environment in relation to the motion measurement target. Knowing the locations in each coordinate system facilitated the conversion between the anatomical coordinate system of the CT-Scan and the Optotrak coordinate system. As a result, a digital, kinematic link was created between the radiopaque spheres and their respective targets attached to the same vertebrae. This link allowed the anatomical parameters resulting from the interaction of adjacent vertebral bodies to be driven by each vertebrae's captured motion.

The specimen underwent quasi-static flexion-extension motion (8 Nm to -5.5 Nm, respectively; 0.135 Nm/sec) while mounted on a six component load cell (Model MC3A-6-1000, AMTI Multi-component transducers, AMTI Inc., Newton, MA, USA) measuring applied forces and moments.

4.2.2 Kinematic Parameters

The following kinematic parameters are a selection of key descriptors for spinal motion which were assessed in this study. These parameters form the basis for quantitatively comparing the accuracy of interpolation:

Helical Axis of Motion (HAM):

Using the methods described by Daniilidis [16] for dualquaternions, HAM parameters were calculated for each vertebral body's motion from a reference position, for this study it was the neutral posture, to the discrete postural positions describing its motion. It is important to note that there must be at least 3° of rotation about the HAM axis for an accurate calculation of the HAM parameters [54, 55]. A least-squared-error approach is used to calculate the motion between the reference position and current posture to minimize the error the HAM parameter calculations due

to random sensor noise. The locations and orientations of the HAM for a given spinal motion segment were expressed in the local reference system. In the case of this study, only rotational HAM parameters (HAM-r) was evaluated since the translational component is of similar magnitude to its noise. Since HAM-r is composed of an axis and a rotation, these values were multiplied to create a three-component parameter for comparison. A simple distance comparison of the aforementioned three component vector evaluated accuracy. To verify results with previous literature values, the segmental HAM was used.

Foraminal Area:

The foraminal contour was constructed from the non-planar isthmus of the specimen's superior and inferior vertebral bodies' neural foramen using a custom MATLAB tracing program (Fig. 4.2b). These digitized points were then transformed along with the reconstructed anatomical model to create continuous motion data of the selected points. In order to obtain a planar surface for area calculation, the non-planar contour was projected onto the plane which maximized the foraminal area in the neutral posture. Foraminal area measurements in the neutral posture are detailed in Table 4.2.

Spinal Canal Space:

The spinal canal contour of the superior and inferior vertebrae of each motion segment were acquired by tracing the posteroinferior and posterosuperior edge of the vertebral body respectively along with the superior edge of the lamina (Fig. 4.2c-d). Analogous to foraminal area, the traced points were transformed along with the reconstructed anatomical model. Again, in order calculate area, the points obtained from the spinal canal tracing were projected on to the plane which maximized spinal canal area of the inferior body. Spinal canal measurements in the neutral posture are described in Table 4.2.

4.2.3 Local Coordinate System

A semi-automated process, was used to determine the local coordinate system for a given vertebral body located at the approximate geometric center of its superior endplate (Fig. 4.2a). The

algorithm is divided into three components (Fig. 4.3): (i) identifying the local sagittal plane of the vertebrae, (ii) identifying the local transverse plane, and (iii) determining the origin of the local coordinate axes.

To identify the sagittal plane, the algorithm employs the concept of bilateral symmetry planes (BSP) [65]. Specifically, BSP evaluates the best plane which minimizes the summation of the distance each 3-D point within the vertebral point cloud would be from another 3-D-point if reflected over the plane. In many cases, vertebrae contain anomalies like osteophytes which distort the symmetry represented by the local sagittal plane and this is addressed by using a robust minimization algorithm which accounts for outliers in its minimization. Ultimately, the user verifies the success of the robust BSP when computed on entire vertebrae (Fig. 4.3a). If the computed sagittal plane was incorrect, the user would limit the robust BSP algorithm to just that of the spinous process and main vertebral body.

The local transverse plane is identified as the plane that best fits the superior endplate. The algorithm uses a robust least squares fit of a plane to the superior endplate of the anatomical model which is demarcated by the user (Fig. 4.3b).

Before computing the origin of the axes, the axes themselves are determined from the previously acquired planes. The intersection between the superior endplate plane and sagittal plane represented the posterior-anterior (PA) direction, the caudal-crainal (CC) direction was represented by the normal of the superior endplate plane, and the lateral direction was represented by the cross product between the PA-direction and CC-direction. Finally, the origin of the axes was calculated in two parts by first calculating the weighted centroid of the superior endplate and ultimately determining the closest point on the PA-Axis to the centroid. The resulting closest point was the origin (Fig. 4.3c).

4.2.4 Data Collection and Sampling

Load-motion data were collected at 30 Hz for two full flexion-extension loops. The final extension-to-flexion motion was used to analyze kinematic reconstruction techniques (Fig. 4.4) and down sampled before being interpolated to simulate in vivo data collection.

Two general sampling techniques, moment and angle, and an optimized sampling method specif-

ically for the spine were used to decimate data (Fig. 4.4). General sampling techniques also had subcategories of either equally spaced sampling or flexible sampling around the neutral posture. Originally [25], angular sampling locations were determined individually for each vertebrae relative to their maximum flexion and extension ROM. However, vertebral kinematics is asynchronous as each vertebrae has varying segmental motion rates. Thus, a sampling x-ray would be required to be taken at each vertebrae's sampling location to acquire an identical dataset, which is not a realistically possible. In order to substantially reduce the x-ray sample size and radiation exposure and simulate the process of bi-planar registration which captures all vertebrae in each image as opposed to individually, the sampling frame was determined by averaging the individual sampling times. For example, if the angular sampling location for 25% of the ROM of each vertebrae occurred at 10, 20, and 30 seconds, the final sampling location would be determined to be at 20 seconds, the average of the three sampling times. The sacrum was excluded from the average as it was a fixed to testing apparatus.

Optimized sampling methods adjusted the sample locations based upon known kinematic features of spinal motion, the high flexibility zone (HFZ) and high stiffness zone (HSZ) [20, 64]. In addition to the maximum flexion and extension sample locations, optimized control point locations were equally spaced between a percentage of flexion motion and a percentage of extension motion. For example, the sampling 1/3E-2/3F indicates that the sampling points were equally spaced between one-third the maximum angle of extension and two-thirds the maximum angle of flexion. The sample size for both moment and angular methods varied between 3 and 20 (0.12% and 0.80% normalized rate respectively) while optimized sampling tests were limited between 3 and 9 (0.12% and 0.36% normalized rate respectively).

4.2.5 Reconstruction Accuracy Comparison

Driven by both the original and interpolated datasets, the kinematic parameters were calculated and compared. Interpolated kinematic parameter values were synchronized with the original dataset before analysis. Root mean square error (RMSE) and maximum error (ME) were used to evaluate the kinematic parameter accuracy and were normalized with respect to the maximum change in the kinematic parameter derived from the original dataset, termed normalized room mean square

error (NRMSE) and normalized maximum error (NME) respectively. To minimize the error due to noise, a moving-window mean of 90 frames (3 seconds; Fig. 4.5) was applied to each kinematic parameter in the original dataset for comparison to the interpolated values. A confidence band to quantitatively measure noise was also constructed using a 90 frame moving-window standard deviation (3 seconds; Fig. 4.5).

Bonferroni correction, $pM < \alpha$, was applied individually to each M-comparison two-tailed t-tests.

4.3 Results

Reconstruction accuracy was highly dependent on the kinematic parameter being interpolated due to the derivation of each kinematic parameter's sensitivity to noise. Noise decreased in order of SCA, FA, and HAM-r respectively (Fig. 4.6). Moreover, HAM-r had statistically less noise than both FA and SCA ($p < 0.05$, M = 2). As expected, the success of kinematic reconstruction decreased as the noise increased (NME, NRMSE, $p < 0.01$).

DQHAM interpolation methods provided the best reconstruction for all three kinematic parameters (Fig. 4.7). More specifically, interpolator DQHAM-Time had the lowest error for sample sizes between 4 and 13 for all kinematic parameters (Fig. 4.7). Reconstruction error of interpolator DQHAM-Time became asymptotic around a sample size of 9 for both FA and SCA (N = 9; NME: 4%, 8%; NRMSE: 1.5%, 3% respectively) while HAM-r never plateaued (N = 9; NME: 2.1%; NRMSE: 0.67%).

In order to evaluate general sampling technique accuracy, QHAM results needed to be removed from accuracy calculations due to having significantly larger error than all other interpolation techniques (Fig. 4.7). Once removed, all general sampling techniques provided similar accuracy results for both FA and SCA. Equal angles sampling provided the most accurate reconstruction of HAM-r for sample sizes less than 10 (Fig. 4.8). Similar results occurred when examining general sampling techniques in combination with the best interpolator (DQHam-Time). Evaluating normalized accuracy, HAM-r and FA reconstruction provided reasonable results between sample sizes 7 (NME: 3.7%, 5.0%; NRMSE: 1.6%, 2.4%, respectively) and 9 (NME: 0.8%, 3.5%; NRMSE: 0.4%, 1.5%, respectively) while SCA suffered more from noise in comparison to the former parameters (N = 9;

NME: 7.4%; NRMSE: 2.4%). However, ME and RMSE values provided closely matching results for both FA and SCA (N = 9; ME: $1.8 \pm 0.5\text{mm}^2$, $2.2 \pm 0.3\text{mm}^2$; RMSE: $0.9 \pm 0.2\text{mm}^2$, $0.8 \pm 0.1\text{mm}^2$, respectively).

Optimized feature-based sampling 2/3E-5/6F and 3/5E-5/6F combined with interpolator DQHAM-Time typically improved NRMSE and NME accuracy with respect to general sampling techniques between sample sizes of 7 and 9; however, these improvements were limited (Fig. 4.9).

Clinical analyses show a strong, linear correlation between change in foraminal area and change in segmental motion from the neutral posture (Fig. 4.10). The slope of this correlation decreased in the caudal direction. Maximum change in foraminal area compared to the neutral posture occurred in flexion, and was similar for all segments, approximately 40 mm.

Spinal canal area for this preliminary dataset also had a strong, linear correlation with change in segmental motion for all segments except L4-L5 (Fig. 4.11). The slope for all segments excluding L4-L5 were nearly identical in extension and flexion ($\Delta\text{SCA} \approx 4.4\Delta\text{SegAngle}$); L4-L5 had a quadratic correlation, although its slope between full extension and approximately three degrees of flexion was similar to the others.

The HAM could be categorized into two distinct groups, flexion motion and extension motion. Extension helical axes were aligned in the coronal plane while flexion helical axes were slightly out of plane (Fig. 4.12). Primarily, these motions rotated about at axis perpendicular to sagittal plane (Fig. 4.13). HAM data derived near zero segmental angular change was unstable due to inaccuracy in evaluation of HAM with limited angular change.

4.4 Discussion

The purpose of this study was to assess the effectiveness of motion reconstruction techniques in evaluating kinematic parameters for use with in vivo bi-planar x-ray imaging. Building upon previous studies (Coburn and Crisco, 2005; Goodsitt et al., 2016) which exclusively discussed motion reconstruction success of rigid body position, this study investigated the interpolation sensitivity of HAM-rotation, foraminal area, and spinal canal area. Concurrently, this study provides a new method for evaluating in vivo spinal canal area and preliminary in vitro data.

4.4.1 Kinematic Parameters

The kinematic parameters chosen were selected based upon their clinical significance and in order to demonstrate the effectiveness of the 3-D kinematic analysis technique to assess morphological interactions of the spine such as HAM-rotation [18, 19, 21, 61] foraminal and spinal canal stenosis [13, 14, 50]. While HAM-r is only dependent on movement of an individual rigid body, FA and SCA rely on the successful reconstruction of two rigid body motions (joint rigid body mechanics). Subsequently, more relative noise was visible in both FA and SCA original datasets. This was also reflected in the larger interpolation reconstruction error of each parameter which occurred when sampling points existed on the extrema of the confidence band (Fig. 4.5). Sampling on the extrema of the confidence band forces the interpolation algorithm to approximate the motion such that it would exist on the extrema rather than the mean, thus incurring larger error.

Results for both the HAM and FA relationships matched previous literature findings. As expected [19], the primary component of the HAM during flexion-extension motion was about the lateral axis with small amounts motion about the other axes. Typically motion waned about the other axes as the magnitude of the change in segmental angle increased and could be a measure of the instability within the joint, although it was previously mentioned that the flexion-extension HAM, as oppose to the lateral bending HAM, may not accurately describe disc degeneration due to elevated interaction of ligaments and facets clouding the instability of the disc [19].

FA was shown to have a linear correlation with decreasing slope when traversing the vertebral segments caudally expanding on a previous study which only illustrated L2-L3 and L4-L5 correlations but with congruent results [34]. Further, the decrease in foraminal area from L2-L3 to L5-S1 matched previous authors' descriptions [34]. For three of the four segments, both left and right FA had closely paired results. L5-S1 provided two similar, but distinctly different results for left and right FA which may have resulted from the difficulty in demarcating the foraminal contour on S1.

In vitro SCA for an entire flexion-extension kinematic dataset had not previously been described in literature. However, the results in this study matches previous literature's discrete posture measurements of SCA, describing decreased SCA in extension [50]. For all but one segment, change in SCA increased linearly with respect to a positive change in segmental angle, thus indicating that more flexion range of motion reduces the chances of a spinal canal stenosis. In these cases, the

superior vertebrae's spinal canal contour is typically situated posteriorly with respect to the inferior vertebrae's contour allowing for a reduction in canal stenosis. For the case of the L4-L5 segment, the anterior edge of the superior spinal canal was only slightly more posterior than that of the inferior body. During flexion, the superior contour would extend past than the inferior contour causing a reduction in area.

4.4.2 Accuracy Comparison

Since all interpolated transforms were calculated relative to the neutral posture, QHAM interpolation methods had increased error around the neutral posture for its interpolated datasets. This is likely attributed to the continuously decreasing range of motion over which the HAM is calculated [54, 55]. More specifically, the separation/synchronization process of rotation and translation requires an accurate representation of the helical axis to calculate the axis origin which may be magnifying this issue (Fig. 4.14). Additionally, QHAM produced more undulations which Coburn and Crisco warned could occur without their manual tangent, continuity, and bias adjustments [11]. Consequently, QHAM had substantially more error in FA and SCA calculations than the other interpolators.

Interpolation method DQHAM-Time consistently produced the best motion reconstruction for calculating simple [25] and complex kinematic parameters. However, general sampling techniques failed to distinguish themselves when comparing FA and SCA reconstruction error. Considering HAM-r produced distinguishable results between general sampling techniques with the same dataset, further optimization of the FA and SCA calculation may also produce separable results. In either case, equal angles sampling is the recommend pair to DQHAM-TIME for motion interpolation as it produced the best results for HAM-r, was not comparably worse than other sampling techniques for FA and SCA, and was previously shown to be the best solution for positional data reconstruction [25]. Feature-based sampling 2/3E-5/6F and 3/5E-5/6F provide the best results for sample sizes between 7 and 9, but would be difficult to implement for in vivo studies.

4.4.3 In Vivo Application

Minimizing the sample size required for bi-planar registration is critical to reducing radiation exposure, but is done so at the expense of resolution. Results from the combination of the best interpolator, DQHAM-Time, and general sampling technique, equal angles sampling, suggest that HAM-r and FA reconstruction could be done successfully for sample sizes between 7 and 9 x-rays. In combination with feature-based sampling 3/5E-5/6F, reconstruction error could be reduced further for these smaller sample sizes, but as previously mentioned, this technique would be difficult to implement in vivo. Despite SCA's sensitivity to noise as illustrated by its NME, these are values relative to the total change in area. Nominal values were as little as 2.2 ± 0.3 mm^2 for the continuous dataset which is a substantial improvement upon previous static techniques and represent less than 0.7% of the average maximum SCA of these segments. Moreover, SCA reconstruction produced reasonable NRMSE results.

4.4.4 Limitations and Future Work

Only one specimen and only four motion segments (L2-S1) were analyzed to evaluate kinematic parameters. The discussion on the kinematic parameters must be understood as a preliminary dataset, especially when discussing SCA where limited previous work has been completed. The 3-D CT-based model technique presented does not capture the effect of soft tissue stenosis in the calculation of FA and SCA Additionally, only three kinematic parameters were evaluated, new parameters may have varying degrees of sensitivity to interpolation. There are also limitations regarding the interpolation methods discussed previously [25].

Sensitivity of the kinematic parameter calculation to noise in the original dataset limited the assessment of reconstruction methods, most notably for general sampling techniques. Future work could investigate first smoothing the original motion dataset before comparison, however this would not reflect the noise inherent to bi-planar registration which would not be feasible to smooth due to limited sample size. Altering the kinematic parameter calculation method may be a solution as well if it reduces its sensitivity to noise.

4.5 Conclusion

Using previously developed reconstruction methods, this study was able to evaluate multiple techniques sensitivity to the reconstruction of the complex kinematic parameters: HAM-r, FA, and SCA. Additionally, a new method to evaluate SCA was described and a preliminary dataset discussing SCA was provided. Sensitivity of the complex kinematic parameters' reconstruction due to noise illustrated the importance of choosing a bi-planar registration technique which does not sacrifice accuracy for speed. Ultimately, all three kinematic parameters were reproducible from low sample sizes suggesting their applicability to in vivo studies.

4.6 Acknowledgments

Financial support was given by the Small Projects in Rehabilitation Research (SPiRE) Award from the VA Rehabilitation R&D.

4.6.1 Conflicts of Interest

There were no conflicts of interest associated with the presented work by any of its authors.

4.7 Figures

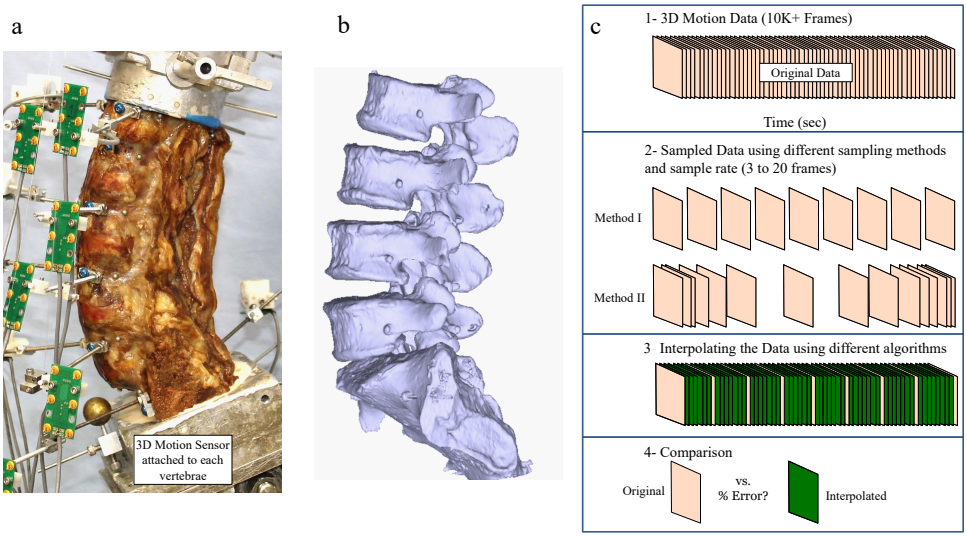

Figure 4.1: a) Lumbar specimen testing setup. b) 3-D reconstruction of the lumbar specimen. c) Demonstration of motion data decimation and interpolation. The method goal is to find an algorithm and sampling method which gives the least error at the minimum sample rate.[1]

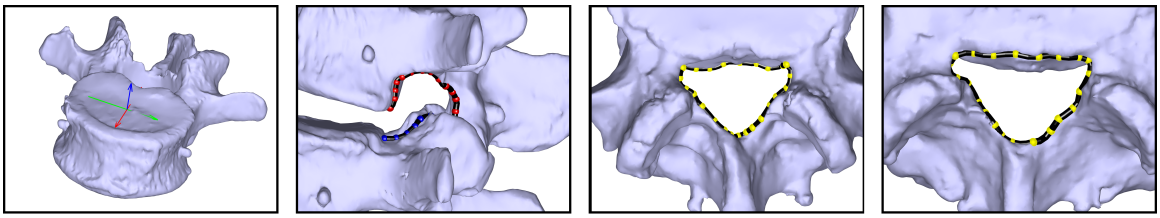

Figure 4.2: Illustrations of the L2-L3 a) local coordinate system, b) superior and inferior formainal canal tracing, c) inferior vertebrae spinal canal tracing, and d) superior vertebrae spinal canal tracing.

[1]This artwork was published in Journal of Biomechanics: Jeremy E. Goodsitt, Robert M. Havey, Saeed Khayatzadeh, Leonard I. Voronov, and Avinash G. Patwardhan. Interpolation of three dimensional kinematics with dual-quaternions. Journal of Biomechanics, 2016. http://dx.doi.org/10.1016/j.jbiomech.2016.10.028 and reprinted with permission from Elsevier.

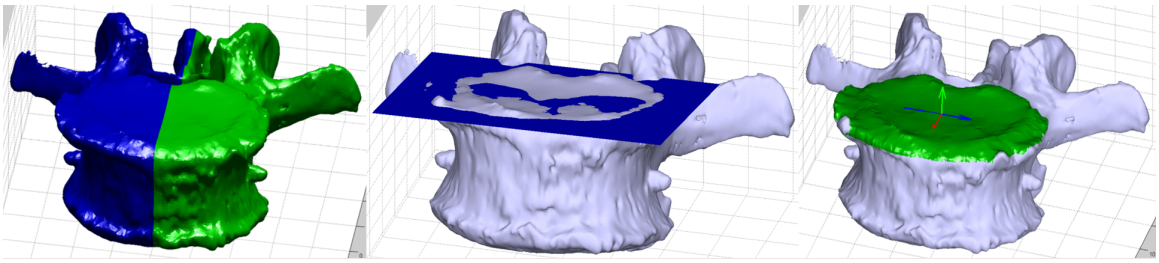

Figure 4.3: Algorithm illustration for determining the local coordinate system of the vertebrae. The three step algorithm depicted as follows: (i) the evaluation of the computed sagittal plane, (ii) evaluation of the transverse plane on the superior endplate, and (iii) the origin of the local coordinate system calculated from the centroid of the superior endplate and the AP sagittal line on the superior endplate.

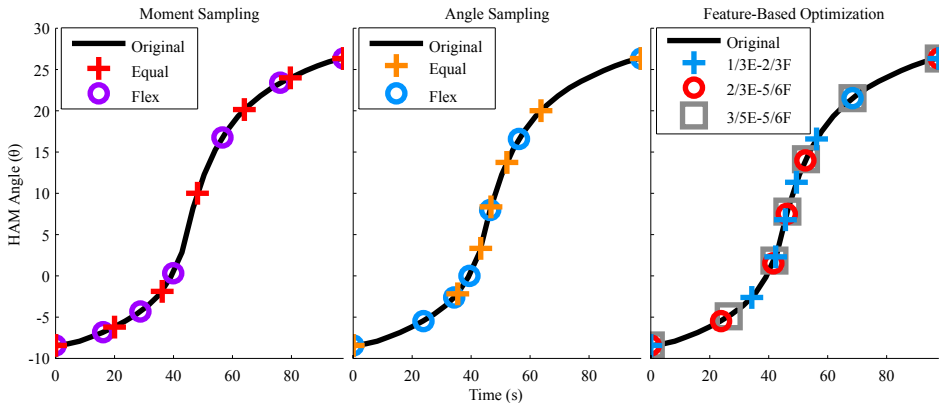

Figure 4.4: (a) Moment, (b) angle, and (c) and feature based optimized sampling for the L2 vertebra (interpolation N = 7).[1]

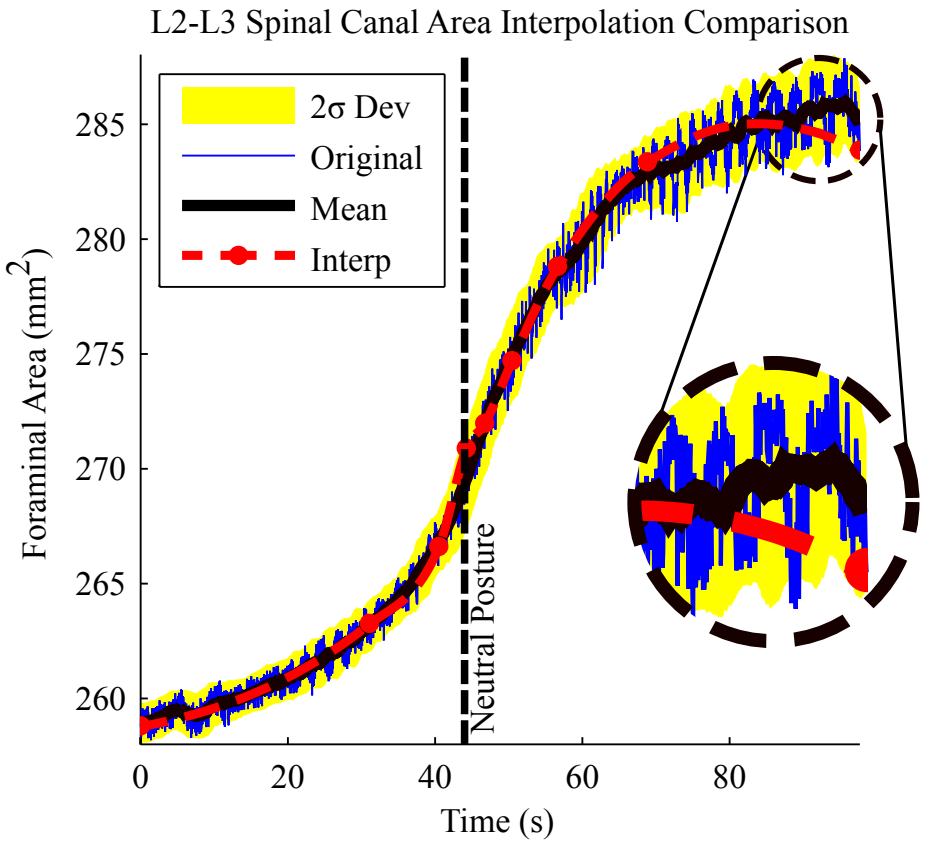

Figure 4.5: Illustration of the L2-L3 foraminal area reconstruction and the effects of noise (N=7).

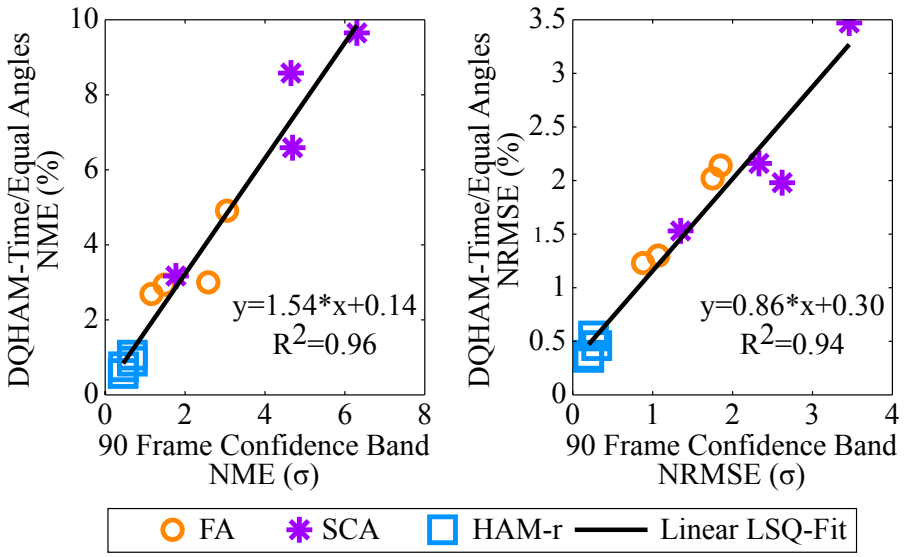

Figure 4.6: A comparison between accuracy and noise in calculating the complex kinematic parameters FA, SCA, and HAM-r.

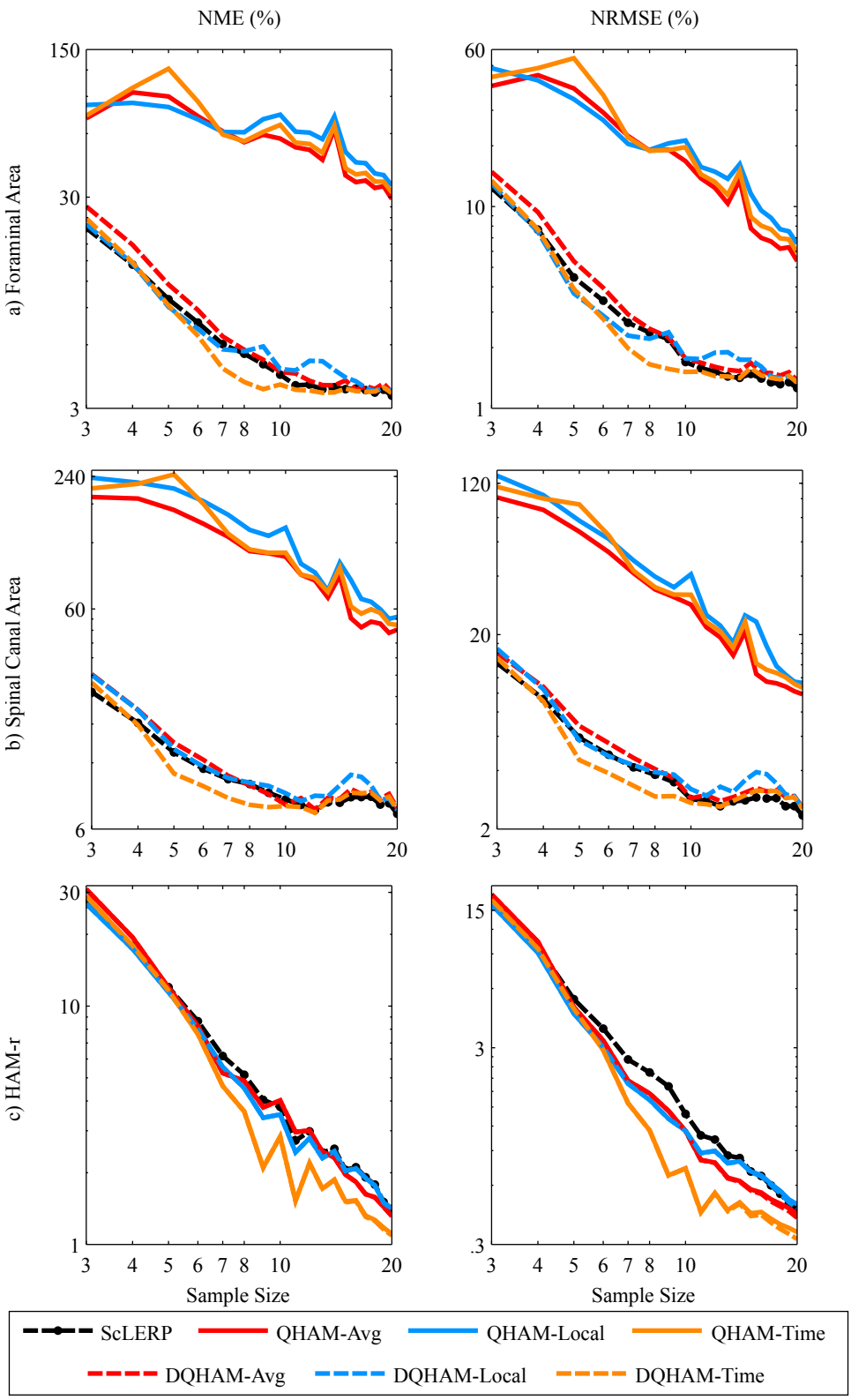

Figure 4.7: Interpolator accuracy comparison of normalized root mean squared error vs. sample size for all kinematic parameters.

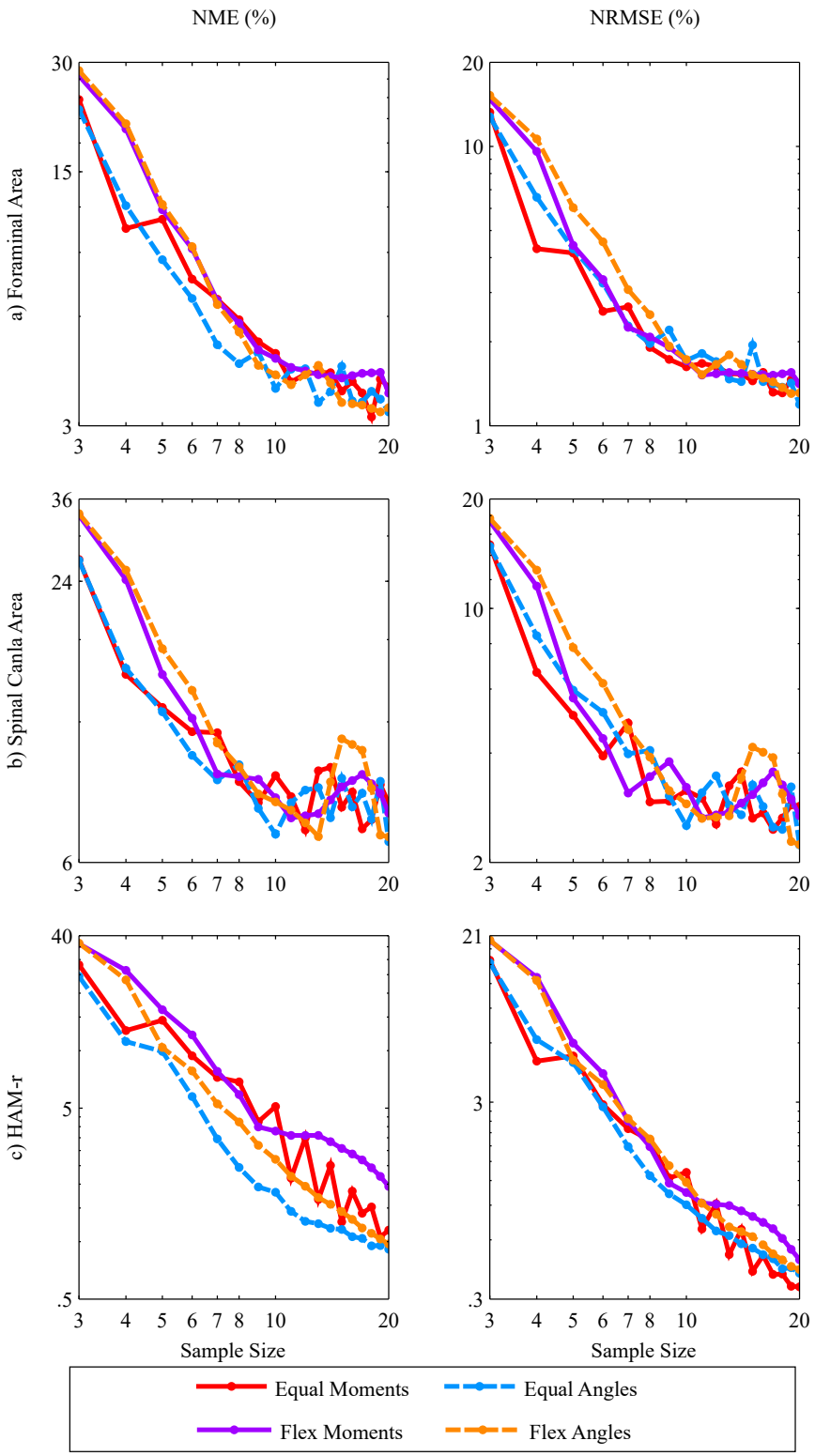

Figure 4.8: Comparing sampling techniques NRMSE and NME accuracy against sample size for all kinematic parameters. However, QHAM interpolators were not included since their results were significantly worse than the other interpolation techniques.

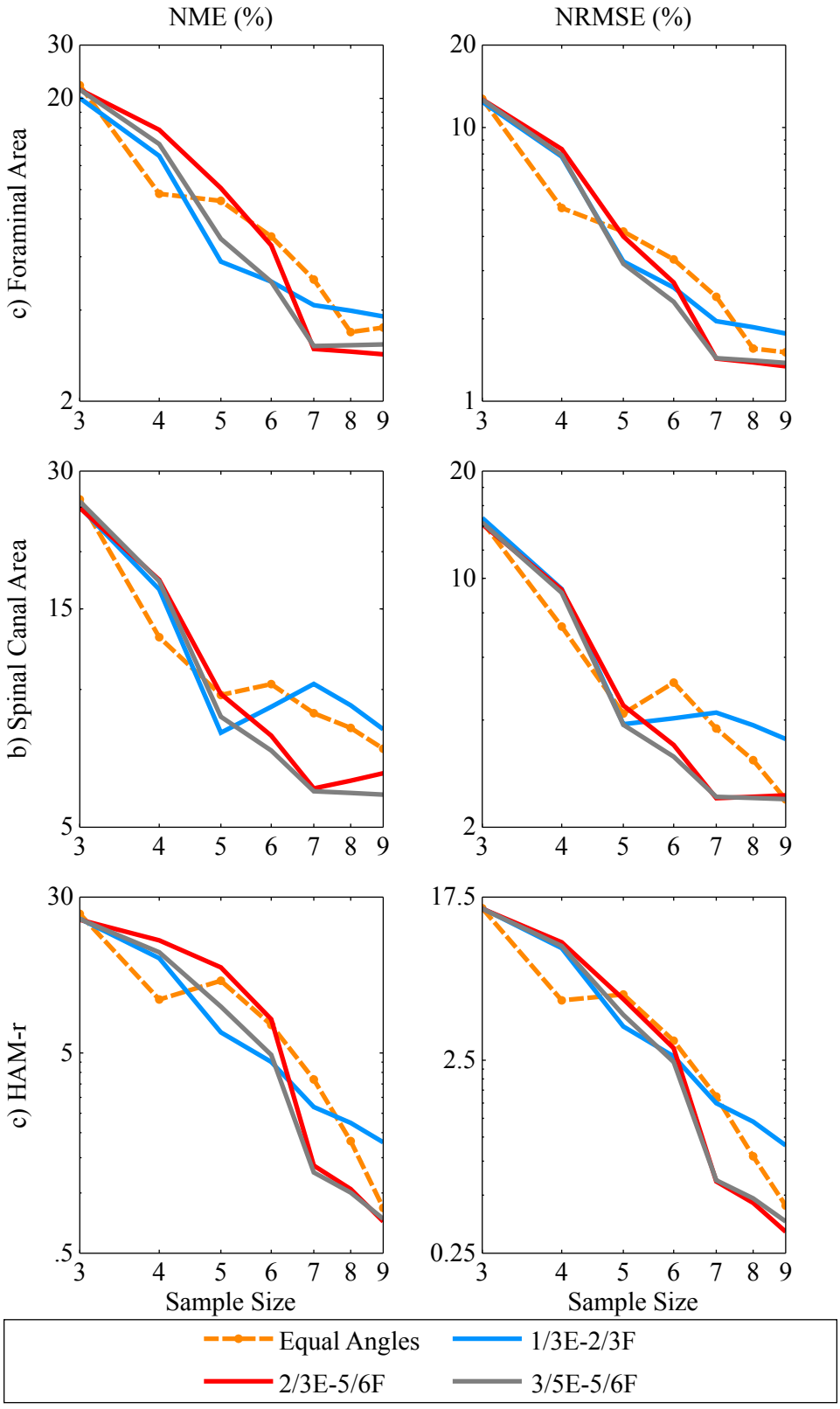

Figure 4.9: Comparing optimized, feature-based sampling techniques with the general sampling technique, Equal Angles, for NRMSE and NME accuracy when using the DQHAM-Time interpolator.

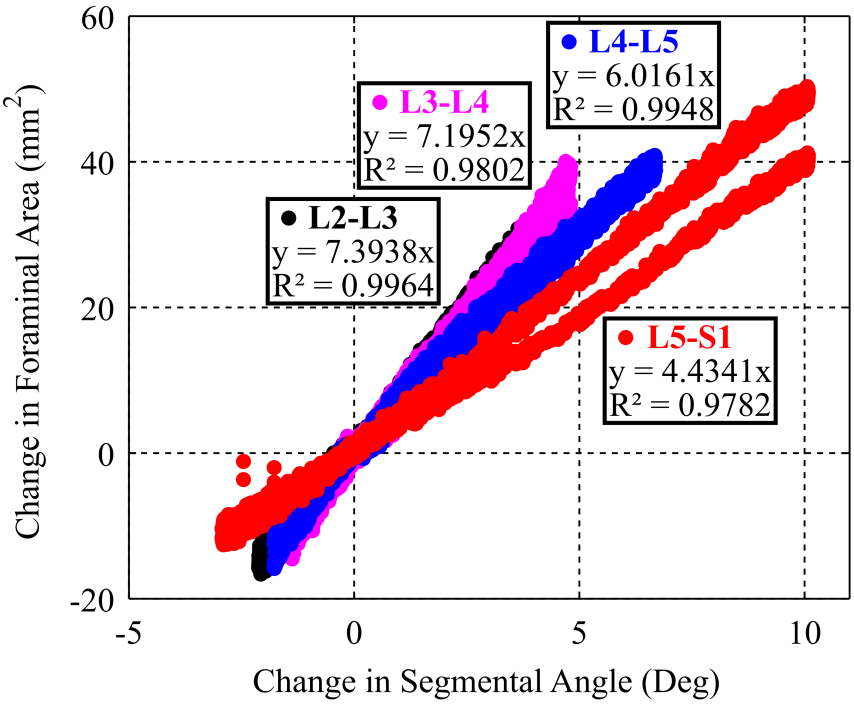

Figure 4.10: Correlation between the change in foraminal area for each segmental joint and its respective segmental motion change relative to the neutral posture. As motion moves from extension to flexion, foraminal area increases.

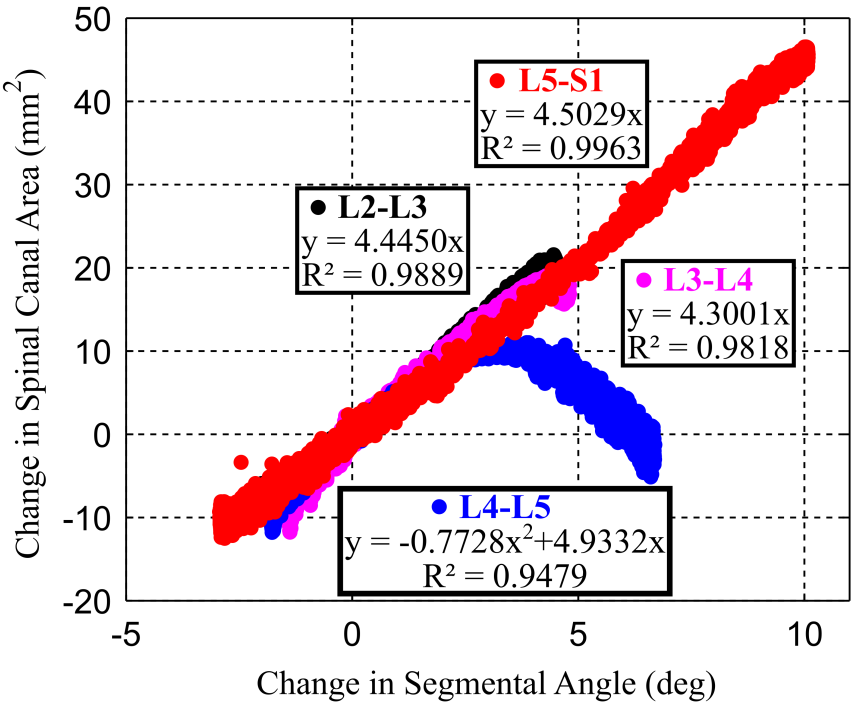

Figure 4.11: Correlation between the change in spinal canal area for each segmental joint and its respective segmental motion change relative to the neutral posture. As motion moves from extension to flexion, spinal canal area typically increases except for the L4-L5 segment.

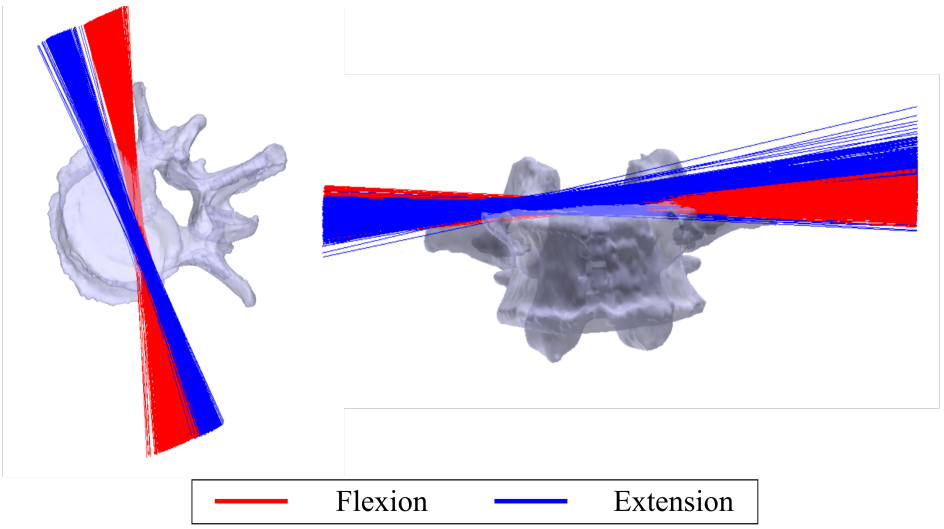

Figure 4.12: Illustration of the differences between the instantaneous axis of rotation for flexion and extension motion of the L2-L3 motion segment.

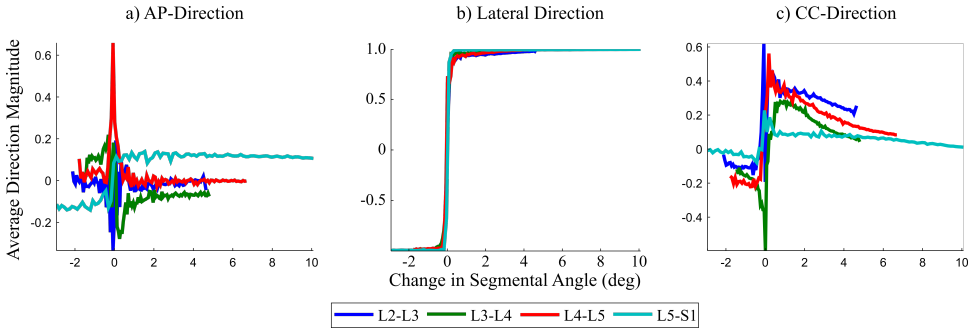

Figure 4.13: Unit vector values for the three orthogonal directions of the instantaneous axis of rotation for the L2-L3 motion segment.

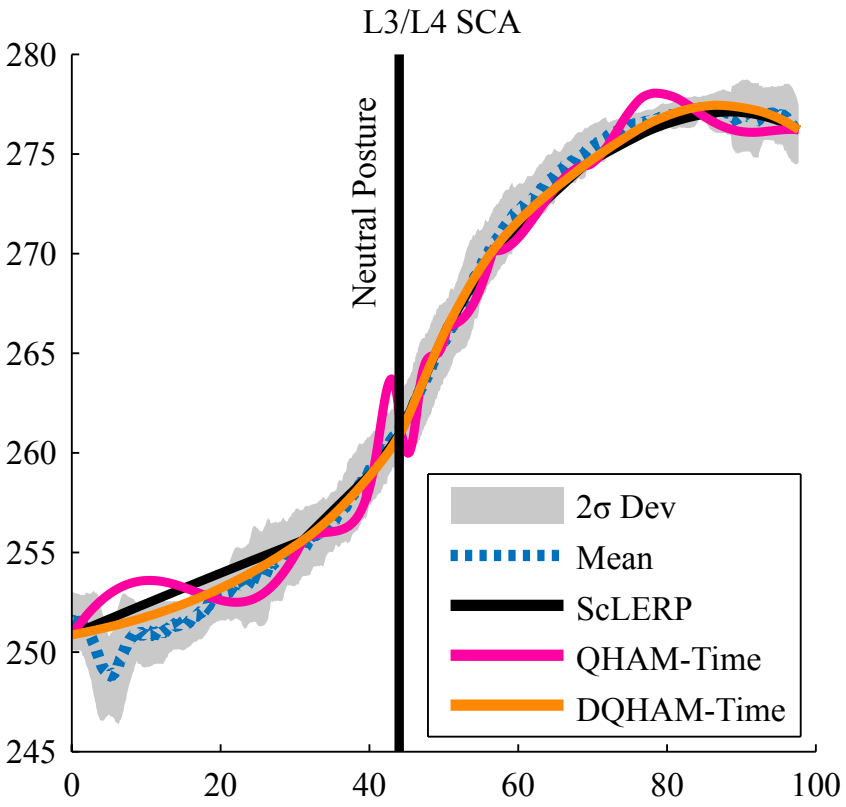

Figure 4.14: Illustration of the differences in interpolation reconstruction using QHAM-Time and DQHAM-Time on the L3-L4 spinal canal area.

4.8 Tables

Table 4.1: Overview of the study's interpolation algorithms, sampling techniques and sizes, accuracy results, and figure/table references.

Interpolation Requirements	Algorithm Options		Optimum Reconstruction Algorithm			Referenced Comparison Figure /Table
Reconstruction Algorithm	ScLERP		DQHAM	Time	**3-Point FD**	Figure 3, 5-8 Table 2
	QHam DQHAM	Tangent Sub Options: **Avg** **2-Point FD** **Local** **3-Point FD** **Time**				
Sampling Method	Moment	**Spacing Sub Options:** **Equal** **Flexible**	Angle	**Equal Spacing**		Figure 2, 4, 7
	Angle	**Equal** **Flexible**				
	Stiffness Zone	Spacing Sub Options: **1/3E-2/3F** **2/3E-5/6F** **3/5E-5/6F**	Stiffness Zone	**3/5E-5/6F**		
Sample Size	3 to 20 (Asymptotic Solution)		Larger increases accuracy Accuracy plateaus 9 samples			Figure 3-7

Table 4.2: Foraminal and spinal canal area (mm^2) in the neutral posture projected onto the plane which maximized its area.

Vertebral Segment	**FA (mm^2)**			**SCA (mm^2)**
	Right	Left	Average	
L2-L3	150.0	149.5	149.7	266.3
L3-L4	130.5	134.0	132.3	258.4
L4-L5	100.0	143.3	121.7	288.7
L5-S1	106.7	131.2	119.0	323.6
Average	**121.8**	**139.5**	**130.7**	**284.2**

Chapter 5

Reducing Radiation Exposure of Bi-planar Fluoroscopic Imaging Techniques for Estimating Spine Kinematic Parameters

5.1 Introduction

Back and neck pain is one of the most prevalent musculoskeletal ailments. In 2012, 24.8% of adults above the age of 18 were reported to experienced lower back pain in the previous three months [45]; and chronic back pain was estimated to cause activity limitation in excess of 7 million adults in 2005 [35]. Both prevalence and complexity of spinal disorders has in part driven the need for enhanced diagnostic and evaluative in vivo techniques such as 2D-3-D registration methods for kinematic evaluation.

While canal stenosis or degenerative disc disease of the lumbar and cervical has attributed to symptomatic low back and neck pathology respectively, current diagnostic techniques have trouble distinguishing symptomatic patients' results from asymptomatic patients [9, 10, 42, 62]. Thus, the complexity in deriving the pathology, evaluating restorative techniques, and developing restorative technology becomes more problematic. Newer diagnostic techniques, ex vivo [25, 34] and in vivo [2, 68], are investigating the role of 3-D patient-specific kinematics in conjunction with morphology as a function of symptomatic spine pathologies. Theoretically, knowledge of the kinematics throughout the full range of motion, compared to traditional techniques which are typically 2-D or static assessments, could provide the necessary indicators which distinguish symptomatic from asymptomatic degenerative spine diseases or instabilities.

In vivo 3-D kinematic diagnostic techniques such as 2-D to 3-D bi-planar registration present strong capabilities for assessing spinal kinematic parameters, but come with tradeoffs between the amount of patient radiation exposure and a complete patient-specific kinematic description. For example, two prominent bi-planar registration techniques differ by either taking radiographic

images only at selected postures [40,43,44,56,67,68] versus a continuous set at 30 Hz for three seconds [1–7], potentially affecting the accuracy of the diagnostic. However, interpolation algorithms can be used to reduce radiation exposure [11, 25], but newer interpolation techniques have yet to be evaluated on bi-planar registration datasets in evaluating spinal kinematic parameters.

The purpose of this study had two primary components: (1) to provide and discuss a new, diagnostic bi-planar registration method utilizing interpolation to reduce radiation for spine kinematic parameter assessment and (2) to provide ex vivo kinematic data describing several spine kinematic parameters during flexion-extension and lateral bending motions. These parameters include the helical axes of motion (HAM), foraminal area (FA) and spinal canal area (SCA). To the best of the author's knowledge, no data has previously been presented for a continuous description of FA or SCA throughout lateral bending spinal motion.

5.2 Methods

Accuracy of the proposed spine kinematic diagnostic technique (Section 5.2.5) in evaluating spine-specific kinematic parameters was validated against an ex vivo kinematic assessment technique ("Gold Standard"; [34]) . Simultaneous collection between the two kinematic assessment techniques acquired flexion-extension and lateral bending motion data for both lumbar (L2-S1) and cervical (C4-T1) cadaveric specimens. 3-D specimen models generated from CT-scan data were driven by the anatomy's motion generated by each technique within their respective coordinate systems using custom MATLAB (Mathworks Inc., Natic, MA, USA) scripts. An interpolation algorithm [25] was applied to the proposed bi-planar technique to convert discrete motion data into a continuous dataset for comparison to match that of the Gold Standard technique, acquired at a high frequency. Kinematic parameters were derived from the two motion datasets and compared. An overview of the technique can be seen in Fig. 5.1.

5.2.1 Specimen Setup

The experimental testing was be performed using **eight** fresh-frozen human cadaveric specimens, **four each** of cervical (C3-T1) and lumbar spines (L1-Sacrum) of adult male and female donors 40-65 years of age [58], consistent with the most common age group of patients with low back and

neck pain. Specimens were radiographically screened to exclude those with bridging osteophytes, since the goal of the study was to develop a motion assessment technology. However, one cervical specimen was required to be removed due to registration complications of the Gold Standard technique.

Four to six aluminum spheres (1.6 mm radius) were rigidly fixed to each vertebra prior to CT scanning. These spheres were placed such that no three were collinear. General locations were on the anterior of the vertebral body, lateral vertebral body, bilaterally on the lamina and on the spinous process. CT-scan data (LightSpeed VPT, GE Medical Systems; $0.293 \times 0.293 \times 0.625$ mm) were acquired for each specimen.

5.2.2 3-D Specimen-Specific Model

The 3-D specimen anatomy was constructed from CT scan data (LightSpeed VPT, GE Medical Systems) ($0.293 \times 0.293 \times 0.625$ mm). The Gold Standard kinematic data and the bi-planar registration method used the identical CT model, limiting potential sources of error in quantifying the differences in accuracy between the two techniques.

Reconstruction of the CT scan data was conducted using commercially available software (Mimics, Materialise Inc., Plymouth, MI). The various anatomical structures were discriminated based on intensity differences observed in the medical images. In CT imaging, the differences in x-ray attenuation of the various anatomical structures show up as voxel-to-voxel differences in image intensity measured in Hounsfield units (Voxels are the 3-D equivalent of 2-D pixels).

After identifying the vertebral structures in each slice of the CT images using a combination of automatic intensity based thresholding and manual image masking, 3-D models (STLs) of each vertebrae were reconstructed using Mimics's built-in marching cubes algorithm. Each individual sphere was also segmented and their location within the CT coordinate system was recorded.

5.2.3 Experimental Setup

The most cranial and caudal vertebrae were anchored in aluminum cups using bone cement and pins. The specimen was secured in a pure moment kinematic testing apparatus at the caudal end and was free to move in any plane at the proximal end. The caudal specimen cup was mounted to

a multi-component load cell (Model MC3A-6-250, AMTI Inc., Newton, MA) to measure reaction moments which were used as feedback to the control computers (Fig. 5.2). Optotrak optoelectronic rigid body targets containing six IRED's each were rigidly secured to each vertebral body.

For flexion-extension testing, the kinematic range of motion was under load control at a constant rate of 0.14 Nm/sec for lumbar and 0.03 Nm/sec for cervical spines resulting in motion from extension to flexion in approximately 100 seconds. For lateral bending, the constant load control rate was of 0.12 Nm/sec for lumbar and 0.03 Nm/sec for cervical spines occurring over 100 seconds. However, the loading rate varied slightly for each experimental setup. Specimen loading was applied using an apparatus capable of delivering pure moments in all three planes of motion while load control feedback is obtained from the multi-component load cell at the specimen base [34].

Bi-Planar Fluoroscopy

Two C-arms (OEC 9800 and OEC 9900, GE-OEC, Salt Lake City, UT) were utilized to collect the bi-planar radiographs. Due to setup constraints of the Gold Standard kinematic assessment technique [34], the C-arms were aligned approximately horizontal with an approximate angle of 90° between them for the flexion-extension and lateral bending protocol.

Distortion Correction

A perforated copper sheet 35 cm x 35 cm with 1.6 mm holes evenly spaced every 12.6 mm was placed on the image intensifier of both fluoroscopes and aligned with the horizontal. Images of grids were taken and processed to acquire the coordinates of each grid hole in the distorted images. A transformation between an undistorted representation of each grid and the distorted grid-hole coordinates is used to correct all subsequently acquired images for each C-arm. These distortion correction polynomial algorithms are custom written using MATLAB.

Calibration

A calibration cube (90 mm on a side) was used to calibrate the two fluoroscopes' relative geometry and establish parameters of the virtual bi-planar fluoroscopic imaging environment needed for data analysis (Section 5.2.5). With 20 radiopaque spheres equally distributed along its struts (Fig. 5.3a),

the cube was placed in the common field of view of the two fluoroscopes and imaged. The resulting images (Fig. 5.3b) were used as input to custom written MATLAB software and MDLT software provided by Tomislav Pribanic [59] to calculate the precise position and orientation of the x-ray sources and detectors of both C-arms [29]. Using the image and cube coordinate systems, a virtual camera environment was created to simulate the experimental setup for bi-planar registration (Fig. 5.4).

5.2.4 Testing Protocol

Prior to kinematic testing, the radiopaque spheres, which were rigidly attached to each vertebral body and visible on the CT scans, were registered in relation to the optoelectronic target attached to their respective vertebral bodies. This relationship made it possible to track the radiopaque spheres throughout the specimens' range of motion.

The specimen was loaded in flexion-extension (lumbar 8Nm-6Nm; cervical $\pm$1.5Nm) and lateral bending (lumbar $\pm$6Nm; cervical $\pm$1.5Nm). For each planar motion the position of the C-arms were located to optimize image registration. Radiographic images were collected every 0.5Nm for lumbar spine and 0.1Nm for cervical spine through the specimen's ROM. The large sample size was later subsampled to find the minimum number of images which allow accurate prediction of the continuous motion of the specimen using the methodology discussed in Section 3.2.

5.2.5 Construction of Specimen-Specific Kinematic Models

The experimental data collected above was used to build and compare the two specimen-specific models: (1) the CT-based Gold Standard model and (2) a CT-based model using bi-planar fluoroscopic image registration.

Specimen-Specific CT-based Gold Standard Model [34]

Using the methodology outlined by Havey et al. [34], the first step in the model creation was to locate each individual vertebrae's location, originally in the CT coordinate system, in the global anatomical reference system associated with the Optotrak system using the set of aluminum spheres. Ultimately, this technique established a transformation matrix between the two coordinate systems

for each vertebrae.

Using custom written MATLAB mathematical transformation algorithms, the motion of the optoelectronic targets were transformed to reproduce motion of the aluminum spheres attached to the specimen in the anatomical reference system. The motion transformation matrices for a given vertebra were used to calculate the new position and orientation of the STL. The result was an animated 3-D representation of the specimen's CT reconstruction moving in response to experimental inputs.

This technique allowed for the continuous measurement of 3-D motion of any anatomical feature or relationship between anatomical features throughout the specimen's arc of motion with a dynamic translational accuracy of 0.14 mm. Using this technology, assessment of the helical axis of motion, foraminal area, and spinal canal area were evaluated as described in chapter 4.

Specimen-Specific CT-based Model Using Bi-Planar Registration

There were two principle differences between this model and the Gold Standard model: (1) the vertebral anatomy was registered in these models using bi-planar fluoroscopy as opposed to surgically attached radiopaque spheres and optoelectronic targets attached to the vertebral bodies, (2) positional data was only collected at discrete specimen postures in contrast to continuous collection in the Gold Standard model. In the following, the details of the modeling methodology is described.

Using bi-planar fluoroscopic images in combination with a reconstructed 3-D volume ('model') of the specimen, movement of the spine was tracked. The basic steps involved in the model-based tracking technique were as follows: (1) obtain 3-D reconstruction of the bone volume from CT scans, (2) determine the geometry of the bi-planar fluoroscopy system (locations of sources and image planes), (3) generate a pair of DRRs by ray-casting through the 3-D model, and (4) determine the position and orientation of each vertebra of the 3-D anatomic model by optimizing the fit of the two DRRs with the corresponding 2-D bi-planar x-ray images Fig. 5.4. This process is repeated for each pair of bi-planar radiographs corresponding to a different posture of the spine. Once the position and orientation of individual vertebrae are known in each posture, the 3-D motion of each vertebra can be calculated.

Before registration occurred, each vertebrae was manually segmented from each x-ray Fig. 5.5).

Occlusions from the Gold Standard technique were removed from the segmentation to reduce registration errors. Additionally, the radiopaque aluminum spheres were also removed from the segmentation so as not to artificially increase accuracy.

A stochastic optimization function [28] rigidly transformed the 3-D volume of each individual vertebra in the virtual bi-planar fluoroscopic imaging environment until the DRRs derived from ray-casting closely replicate the bi-planar x-rays taken during testing. Once the DRR was created, a Gaussian filter was applied to both the DRR and the x-ray in order reduce local minimum solutions. Image intensity based gradient information (GI; [52]) drove the optimization function by maximizing the gradient similarities between the x-ray and DRR. Each GI result was weighted based upon the size of its mask to all other DRR mask sizes for the vertebrae being assessed. The weighted sum of the GI values for the two DRR vs. x-ray image comparisons was the total objective function. Hence, optimization was achieved when the position of the 3-D volume most accurately represents both x-rays in that posture. Manual segmentation of each vertebra in each x-ray image allowed the optimization function to individually register each vertebra in a DRR to itself in the corresponding x-ray. Once the position of the 3-D volume was determined for each posture, the discrete motion of the specimen were calculated in 3-D space.

Once the position of the 3-D volume was determined for each posture, the discrete motion of the specimen was calculated in 3-D space and subsequently interpolated to generate a continuous dataset. Conventional methods that interpolate each variable individually cannot be used when dealing with joint motion data involving rotation and translation matrices. Individual interpolation methods introduce substantial errors caused by violation of mathematical constraints on rotation matrices. Several improved methods of interpolating 3-D rigid body kinematics have been employed in computer graphics research, but their application to in vivo motion analysis is restrictive due to strict conditions on sample spacing and boundary conditions [11]. A new method, derived from dual-quaternions (DQHAM), to interpolate 3-D kinematics was developed specifically for this study [25] and was evaluated in chapter 3 and chapter 4. This technique was used to predict the 3-D spine kinematics in between the discrete data.

Similar to the Gold Standard, this technique also allowed for the continuous measurement of 3-D motion of any anatomical feature or relationship between anatomical features throughout the

specimen's arc of motion and was used to assess the helical axis of motion, foraminal area, and spinal canal area as described in chapter 4.

5.2.6 Data Collection and Sampling

Flexion-extension and lateral bending motion data were collected simultaneously for both specimen-specific diagnostic techniques. For the Gold standard technique, two full loops of motion data were acquired at 30 Hz, however only the final extension-to-flexion and left-to-right lateral bending movement was used for comparison. Concurrently, bi-planar radiographic images were every 0.5Nm for lumbar spine and 0.1Nm for cervical spine during both movements.

Sampling frames were selected as specified by the equally spaced angles technique in chapter 4. However, since bi-planar radiographs were not taken relative to angular motion, each angular sampling frame was matched with the bi-planar image set that was taken nearest the expected time of said sampling frame.

5.2.7 Reconstruction Accuracy Comparison

Since the Gold Standard data and the bi-planar fluoroscopic images were obtained simultaneously, the continuous dataset derived from the interpolation function was compared with that of the Gold Standard. Relative maximum and average error bounds in reconstructing kinematic parameters between the two techniques were used for comparison. Knowledge of the error bounds is important when conducting non-invasive in vivo kinematic assessment of a patient since the actual movement cannot be derived.

Before comparison, interpolated bi-planar kinematic parameter values were synchronized with the Gold Standard dataset. Relative average and maximum error bounds were calculated from the root mean square error (RMSE) and maximum error (ME) and were normalized with respect to the range of the kinematic parameter derived from the Gold Standard dataset. These values were termed normalized room mean square error (NRMSE) and normalized maximum error (NME) respectively. To minimize the error due to noise from the Gold Standard technique, a moving-window mean of 90 frames (3 seconds) was applied to each kinematic parameter. Similarly, noise of the Gold Standard technique was quantitatively measured using a confidence band constructed

using a 90 frame moving-window standard deviation (3 seconds).

Bonferroni correction, $pM < \alpha$, was applied individually to each M-comparison two-tailed t-tests.

5.3 Results

5.3.1 Interpolation of Bi-planar Registration

The maximum error and RMS error differences between interpolation and sampling points were bounded (Table 5.1), illustrating how successful reconstruction of a continuous motion dataset through interpolation required all sampling locations to have accurate registration as well. Successful registration of HAM-r was more common than FA or SCA for each vertebral segment (Table 5.2). Also, LB was shown to have more registration success than FE for each vertebral segment.

Segmental registration success was determined by accurately evaluating all three parameters for a given vertebral segment at all sampling locations for a sample size of 9. For FE bending, only 4 lumbar and 4 cervical vertebral segments out of 16 and 12 respectively were determined successful. Similarly for LB bending, only 5 lumbar and 7 cervical vertebral segments out of 16 and 12 respectively were determined successful. Accuracy of reconstructing these segments through interpolation are shown in Table 5.3. Only one specimen had a successful registration for all of its vertebral segments, but only for LB.

For the cases of successful registration of the lumbar spine, increasing sample size typically reduced each kinematic parameter's maximum and average error except for SCA when undergoing lateral bending motion (Fig. 5.6). However, this was not the case for cervical specimen (Fig. 5.6), where increasing sample size did not affect the accuracy and had the potential to reduce accuracy.

5.3.2 Gold Standard Kinematic Parameter Evaluation

Accuracy evaluation of the interpolated bi-planar kinematic parameter dataset were compared to that of the optoelectronic 3-D CT-based specimen-specific model. A comparison of average values for FA, SCA, and separately HAM-r for the Gold Standard technique are illustrated in Fig. 5.7 and

Fig. 5.8 respectively. FA and SCA values in the neutral posture for cervical and lumbar specimen are shown in Table 5.4 and Table 5.5 respectively. Noise in calculating these values are shown in Fig. 5.9. When normalizing these values to their maximum range, HAM-r had significantly less noise than the other two parameters for both flexion-extension and lateral bending motions ($p < 0.05$, M = 2).

A summary of cervical (Table 5.6) and lumbar (Table 5.7) FA and SCA relationship with the change segmental angular motion relative to the neutral posture was reported. Lumbar angular segmental FE data (Fig. 5.10) had a strong, linearly correlation with FA ($R^2 > 0.90$) and a moderate to strong linear correlation of SCA ($R^2 > 0.50$). Lumbar LB FA versus change in segmental angle was better fit by a quadratic model ($R^2 > 0.50$) as oppose to linear; however, SCA LB did not fit either model for segments L3-L4 or L5-S1. For the cervical spine (Fig. 5.11), only a linear model was used for estimating correlations. FA illustrated moderately strong to strong relationship with change in segmental angular motion ($R^2 > 0.75$), while SCA did not correlate ($R^2 < 0.40$). Translating caudally, the slope of FE FA versus change in segmental angular data decreased for lumbar spine and increased for cervical. Graphically, the segmental curves of LB FA for both cervical and lumbar spine appeared similar (Table 5.7; Table 5.6).

5.4 Discussion

In vivo diagnostic techniques are paramount for both understanding rigid body joint mechanics and developing the restorative technology. A new method for evaluating in vivo lumbar and cervical kinematic parameters was described and compared against an optoelectronic ex vivo technique. Additionally, ex vivo foraminal area and spinal canal area undergone flexion-extension and lateral bending motions were described for cervical and lumbar spine.

5.4.1 Specimen-Specific Bi-planar Registration Comparison

Before detailing the accuracy of the presented registration technique, it is important to understand the sources of error between both the presented and validation technique. Accuracy of the Gold Standard technique was described as 0.14 mm of dynamic translation, during motion capture of the specimen. However, there is additional error for registering the CT-based specimen-specific model

with the optoelelectronic motion tracking system which was measured at 0.40 mm due to the CT voxel size ($0.293 \times 0.293 \times 0.625$ mm) [34]. These sources of error are methodically different than the presented technique in that error of registration is incurred once for each vertebrae as oppose to at every bi-planar sampling location and vertebra for the presented technique. However, the dynamic tracking error is analogous to the interpolation error of this system.

Comparing the two techniques cannot determine whether the best possible bi-planar registration occurred, but rather validates the accuracy of bi-planar in its entirety. As a result, sources of error can only be speculated upon for this study rather than be confirmed. For bi-planar registration, sources include but are not limited to the CT voxel size ($0.293 \times 0.293 \times 0.625$ mm), radiograph resolution (0.31×0.31 mm) and clarity (i.e. vertebrae blur from the dynamic spine motion or out of plane radiographs), vertebral segmentation, the optimization technique or objective function, and determining the virtual camera environment. Vertebral overlap within the radiographs, which can obscure registration, was also a concern due to specimen flexibility and/or C-arm orientation with respect to the specimen.

Specifically to this study, using the optoelectronic model for comparison introduced error due to radiographic occlusion which would not occur in vivo (Fig. 5.5). Occlusions were more severe in the cervical spine due to vertebral dimensions and increased flexibility as illustrated by C4 in Fig. 5.5a. Also, C-arm orientation could not be optimized and was constrained by the optoelectronic load application system to a limited set of oblique angles with respect to the specimen (Fig. 5.2).

Ultimately, validation required the success of both techniques, but implementing both systems simultaneously potentially increased their error. As mentioned previously, registration of the optoelectronic system occurs only once constraining the vertebra and the optoelectronic tracking target as a single rigid body. If any target moved relative to its respective vertebrae, data such as FA and SCA become meaningless. Similarly, once the C-arm system environment becomes rigidly constrained once determined by the calibration cube and any movement of the C-arms would render registration data and therefore all three kinematic parameters meaningless. Due to these limitations and the location of the experiment, acquiring the registration of both systems required a meticulous process, but also one which may have reduced the accuracy of the Gold Standard registration technique.

The results of this study illustrate the difficulty in developing a successful in vivo diagnostic measurement technique, but simultaneously highlight the potential of the described bi-planar technique. Naturally, success of the technique was highly dependent upon the registration success of the sampling locations. Provided the sampling points were successful, Table 5.1 illustrates how all three bi-planar derived kinematic parameters could provide accurate results and would be within a 95% confidence interval of the optoelectronic method. Further, FA bounds may be lower than reported due to potential outliers resulting from confounding factors which were discussed previously.

Even though a majority of the vertebral segments failed to successfully register all three parameters, trends were still identifiable within the successful set of vertebral segments. Foremost, the accuracy of calculating cervical kinematic parameters did not increase with increasing sample size unlike lumbar kinematic parameters. This could result if the interpolated bi-planar dataset was within noise bounds of the optoelectronic dataset, hence sampling size would not impact the results. Similarly, if the sampling registration is not accurate, increasing sample size would also fail to increase accuracy. Provided the former is true, this is an important result as it indicates that only a small sample size is necessary to accurately assess these cervical kinematic parameters while a larger sample size is required for lumbar specimen. For lumbar, accurate reconstruction was achieved for sample sizes greater than 8.

Accuracy of HAM-r was greater for lumbar specimen. Since noise was similar between lumbar and cervical specimen within the optoelectronic system, radiograph occlusions are likely the culprit as they were higher for cervical specimen. Although, this did not seem to impact FA or SCA results for lumbar vs cervical reconstruction accuracy. It is possible these parameters more closely correlate with the translation component of HAM which was not evaluated since values were near the bounds of noise and a more accurate technique would be required to evaluate. Relative to existing techniques, rotational measurement errors were similar. Accuracy of cervical vertebrae orientation was 1.1° for Anderst et al. [4] and 0.7° for Li et al. [43]. Values for lumbar spine were not reported, however accuracy of this technique was lower than the reported cervical values.

FA and SCA accuracy described in Table 5.3 were less than 5% of the neutral posture value (Table 5.4; Table 5.5). FA typically had more accurate results than SCA which was comparable to the results described by reconstructing the Gold Standard kinematic dataset in Section 4.4. Cross-

sectional area of the foraminal nerve root ranges between 9.6 to 33.2 mm^2 for cervical spine [69] and between 8.6 and 11.9 mm^2 for lumbar spine [66]. cervical spinal cord cross-sectional area was 50 mm^2 on average at T1 and 40 mm^2 at S1 for lumbar spine [38]. Hence, the reported average accuracy of FA and SCA were less than 33% of the foraminal nerve root and 10% of spinal cord cross-sectional area respectively.

In summary, interpolating bi-planar registration datasets displayed great potential for evaluating in vivo spinal kinematic parameters. However, more work needs to be done to both refine the technique and better validate the system and is discussed in chapter 6.

5.4.2 Gold Standard Kinematic Parameter Assessment

A continuous dataset describing cervical and lumbar FA during flexion-extension has previously been reported (11 cervical, [3,46]; 6 lumbar, [34]). In both, FA increased from extension into flexion. Lumbar FA relationship to segmental angle was characterized for L2-L3 and L4-L5. This study both confirms and expands upon these datasets with 3 cervical specimen and 4 lumbar specimen, but also is the first study to evaluate FA throughout the lateral bending motion.

Impingement of the foraminal nerve results from a narrowing of the foramen known as foraminal stenosis. Foraminal stenosis has been linked to loss of disc height which reduces the foraminal height and therefore FA [49,69]. Foraminal stenosis can be exacerbated by movement, hence understanding the relationship between FA and vertebral kinematics can assist in explaining foraminal pathologies. FA's linear relationship with segmental angle during FE decreased in the caudal direction, which is consistent with previous lumbar studies [34]. Despite cervical ROM increasing cranially, FA characterized slope increased in the caudal direction may be due canal morphology in conjunction with the dynamic motion. In lumbar spine, segmental ROM was directly correlated to the change foraminal height [34], however cervical foraminal height was shown to be constant between segmentally [46]. Assuming the change in foraminal height remains constant across all segments, a shallower slope would indicate a smaller change in foraminal width which contradicts previous findings [46].

LB FA remained linear for cervical spine, but was more complicated for lumbar. In right LB, the left FA area increased while the contralateral FA decreased and vice versa for left LB; however

for lumbar spine, the contralateral FA discontinued to decrease and remained constant after an undetermined amount of left lateral bending. This is potentially due to a left lateral tilt in the determined neutral posture.

Spinal canal stenosis occurs from a variety of reasons, while most commonly from disc degeneration [60, 63], morphological factors such as osteophyte and cyst formation contribute as well kyphosis [49]. Degenerative changes can lead to cervical kyphosis or instabilities in lumbar segments which may also incur spinal stenosis [49]. This study examines the morphological effects under dynamic loading conditions. Static studies from MRI or CT-scan data have investigated SCA in end ROM, but no previous study has described SCA through a continuous FE or LB movement. LB SCA remained mostly unchanged by dynamic movements, indicating only extreme stenosis conditions are likely impacted by the movement. On average, FE affected SCA more than LB, but more specimen are required to statistically distinguish the two results. Cervical SCA was not able to be correlated to segmental motion with simplistic models, but SCA was shown to decrease in flexion and extension as well as left and right LB. This can be attributed to the superior segment canal extending past, behind, left, or right of the inferior canal. Such motions were also evident in lumbar FE SCA, but for the most part the trends were linear with an increased area in flexion.

5.4.3 Limitations

Only 3 cervical and 4 lumbar specimens were used to evaluate the accuracy of the interpolation of bi-planar registration technique. Moreover, there was a limited set of successfully registered vertebral segments used to evaluate the potential success of the technique.

Validation of the ex vivo kinematic results also requires more specimen. Though it must be noted, when evaluating FA and SCA that canal narrowing effects from soft tissue are not included due to both techniques' models being derived from CT-scan data.

5.5 Conclusion

This study described a new bi-planar registration technique to evaluate in vivo spine kinematics while limiting the x-ray sample size. Despite limited successful registration, the premise of the technique proved possible and continued refinement of the bi-planar registration technique and

accuracy comparison are needed. Additionally, new data presenting FA and SCA undergone LB were described.

5.6 Acknowledgments

Financial support was given by the Small Projects in Rehabilitation Research (SPiRE) Award from the VA Rehabilitation R&D.

5.6.1 Conflicts of Interest

There were no conflicts of interest associated with the presented work by any of its authors.

5.7 Figures

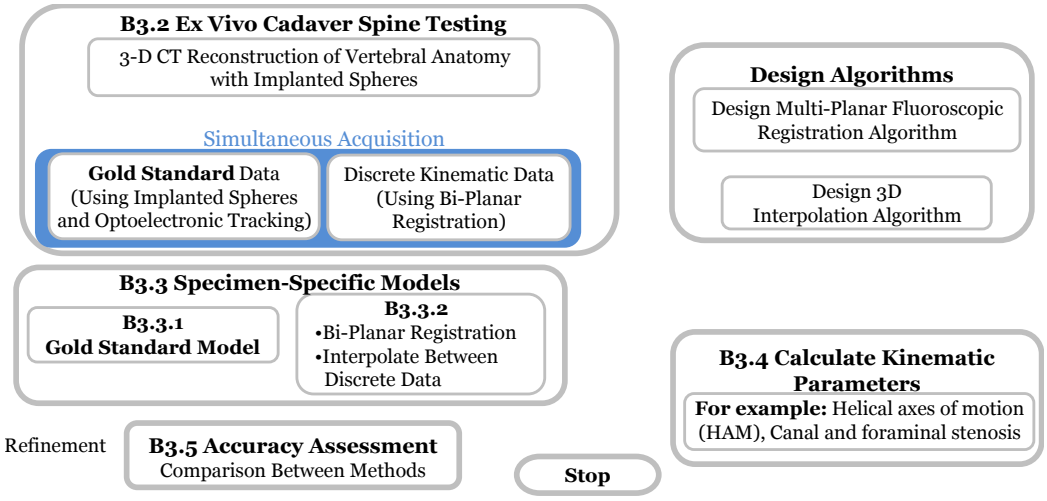

Figure 5.1: An overview of the methodology used to reducing radiation exposure of bi-planar fluoroscopic registration.

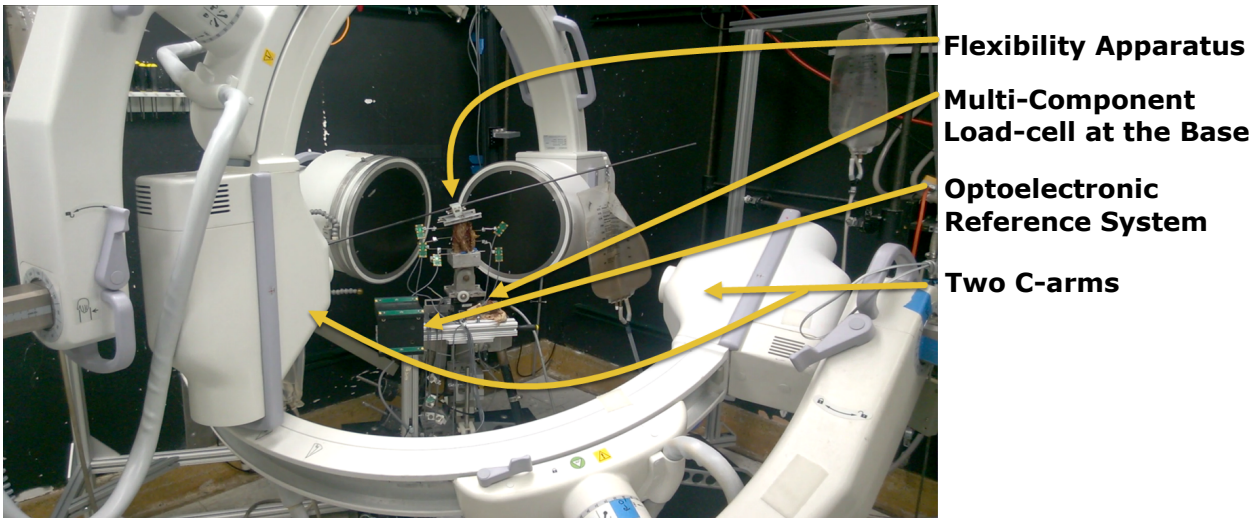

Figure 5.2: Experimental setup for a cervical specimen. The flexibility apparatus, which tests the spine is composed of a long moment arm which have weight applied to it with a system of water bags. At the base of the apparatus is a load cell measuring forces and moments which is fed back to computer controlling the flexibility apparatus. Optoelectronic reference system which defines the coordinate system within which the vertebral targets reside. Two-C-arms horizontally perpendicular to each other.

a) calibration cube

b) x-ray of calibration cube

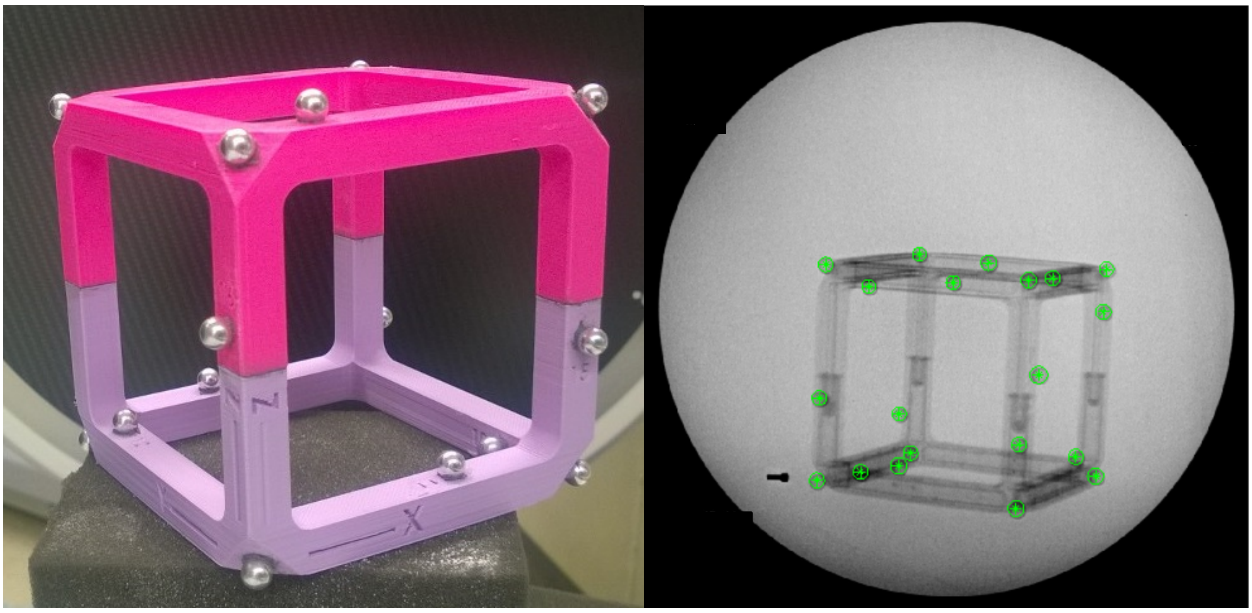

Figure 5.3: a) The calibration cube with 20 radiopaque spheres used to create the virtual camera environment. Each sphere was labeled with its location to easily match to the bi-planar images taken during C-arm environment calibration. b) An x-ray of the calibration cube with all radiopaque sphere locations identified within the image.

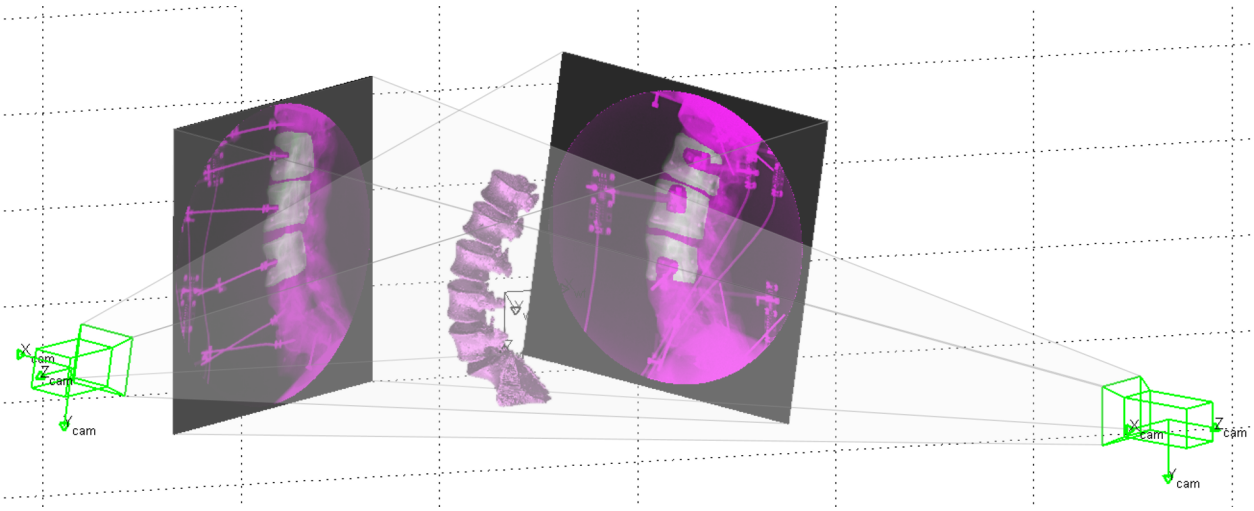

Figure 5.4: Virtual camera environment illustrating the visual fidelity of the registration. Green represents the DRR, magenta represents the C-arm image, and white indicates a strong correlation.

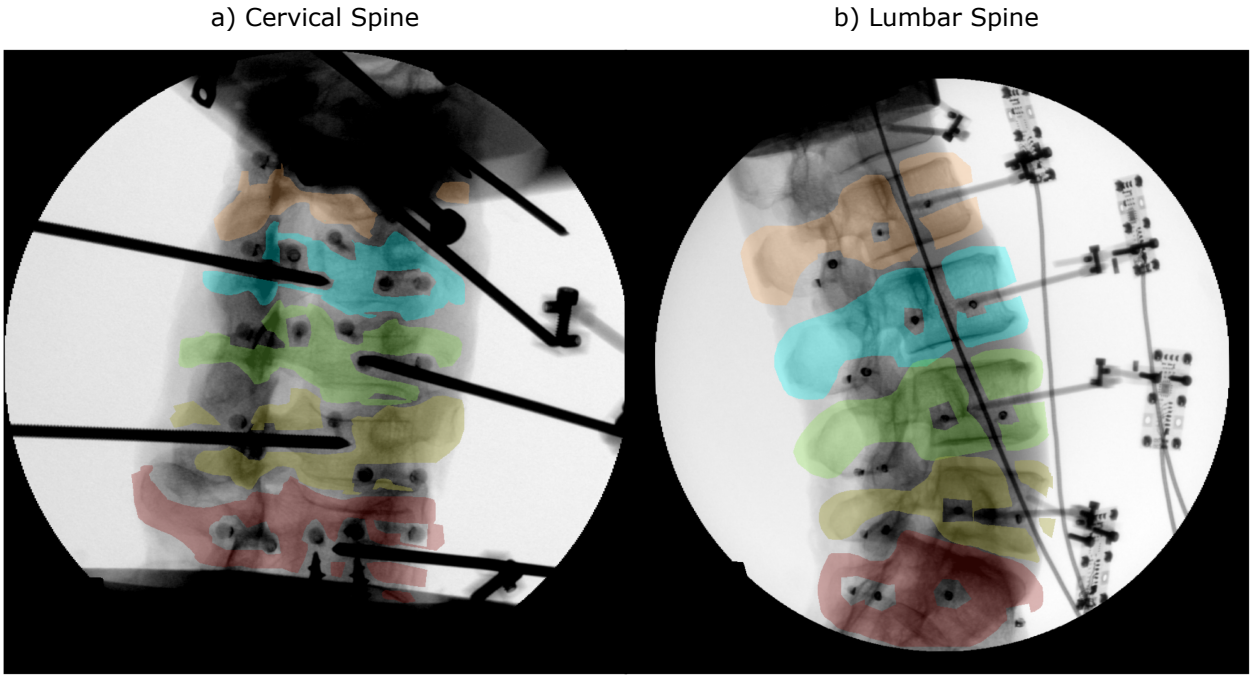

Figure 5.5: An example of verebral segmentaion of bi-planar radiographs for the cervical and lumbar spine. Occlusions due to the Gold Standard technique were more severe for cervical specimen.

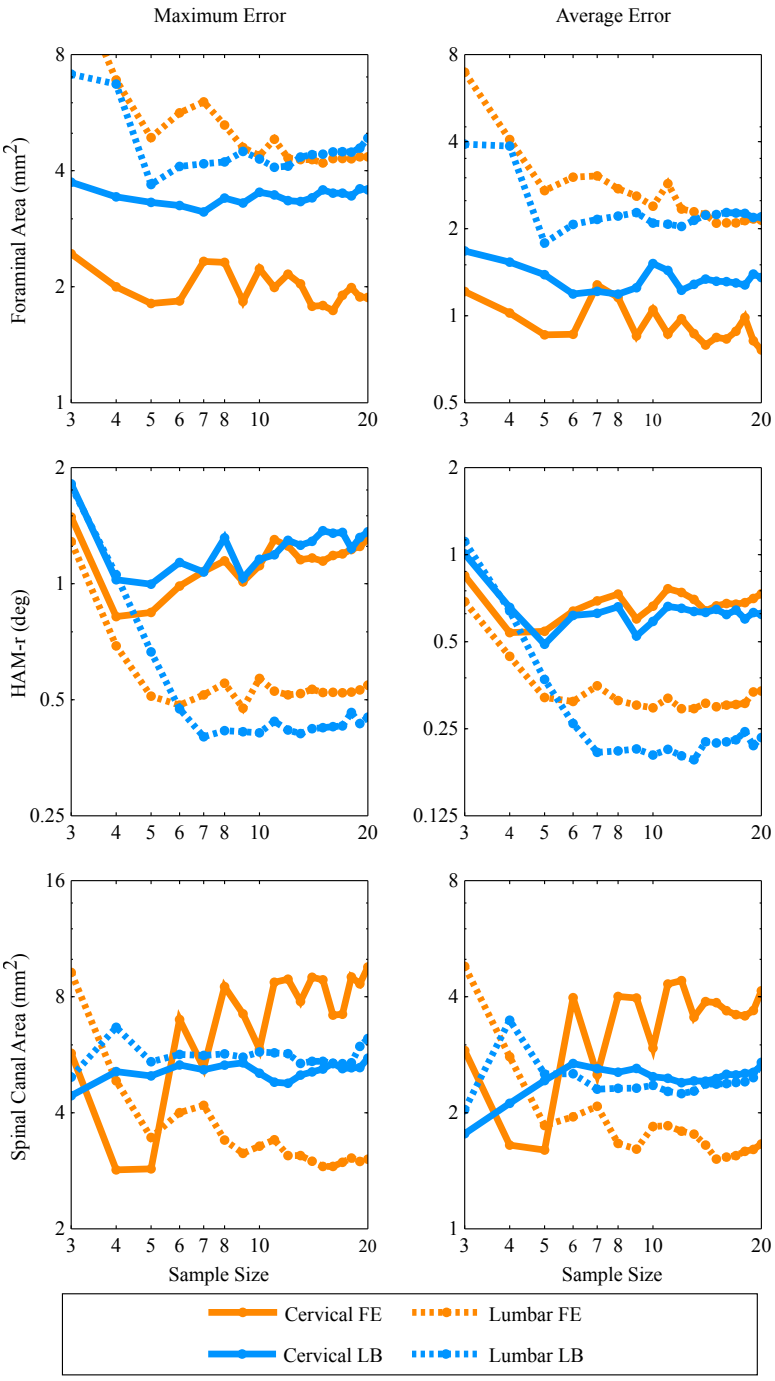

Figure 5.6: Maximum error and RMSE accuracy in calculating the kinematic parameters for vertebral segments which had successful registration of the sampling frame for both lumbar and cervical spine.

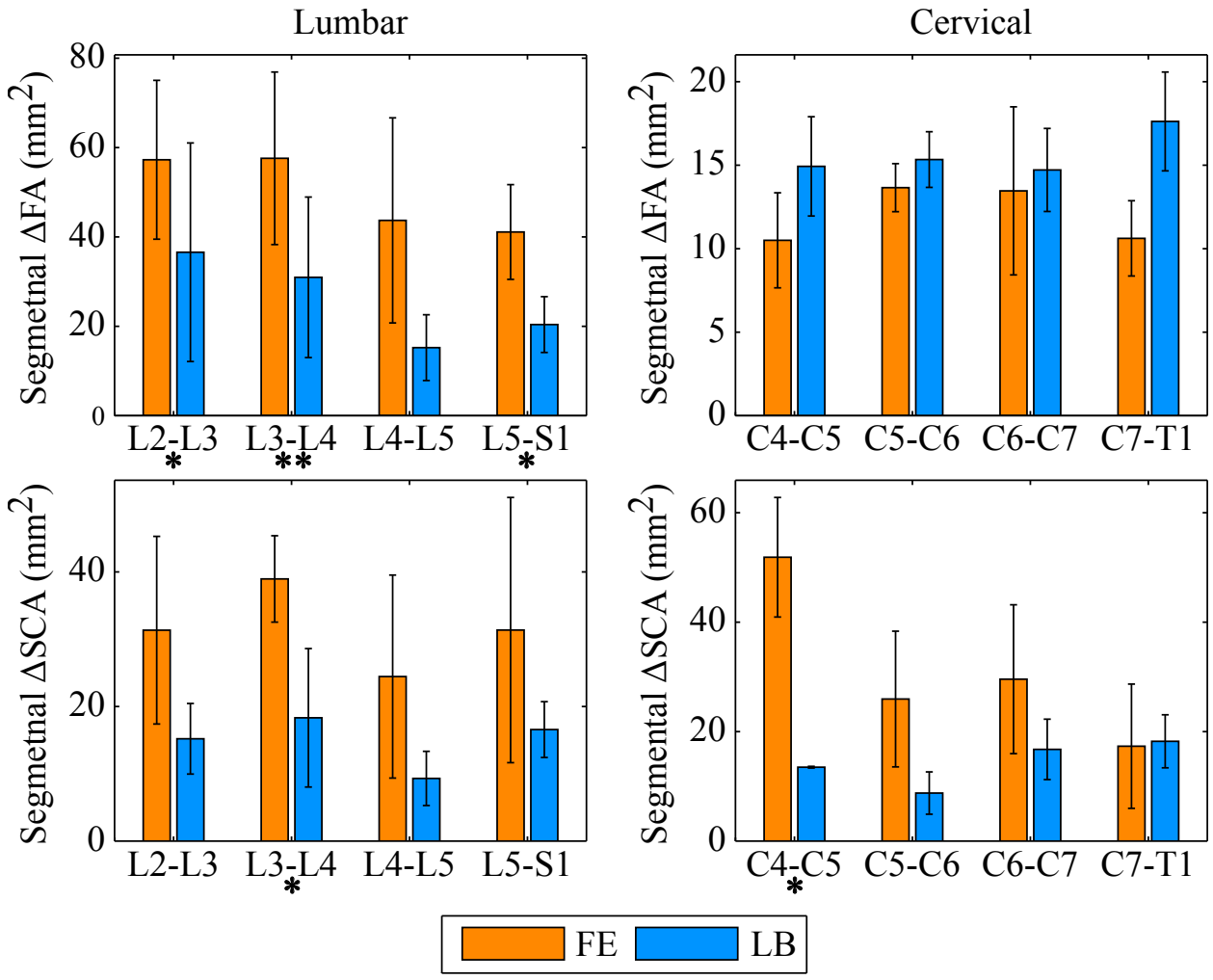

Figure 5.7: Dynamic assessment of foraminal area and spinal canal area during lumbar and cervical extension-to-flexion motion and left-to-right lateral bending motion using the Gold Standard 3-D CT-based specimen-specific model. * or ** indicate that the two motions produced significantly different results ($p < 0.05$, $p < 0.01$ respectively, M = 1).

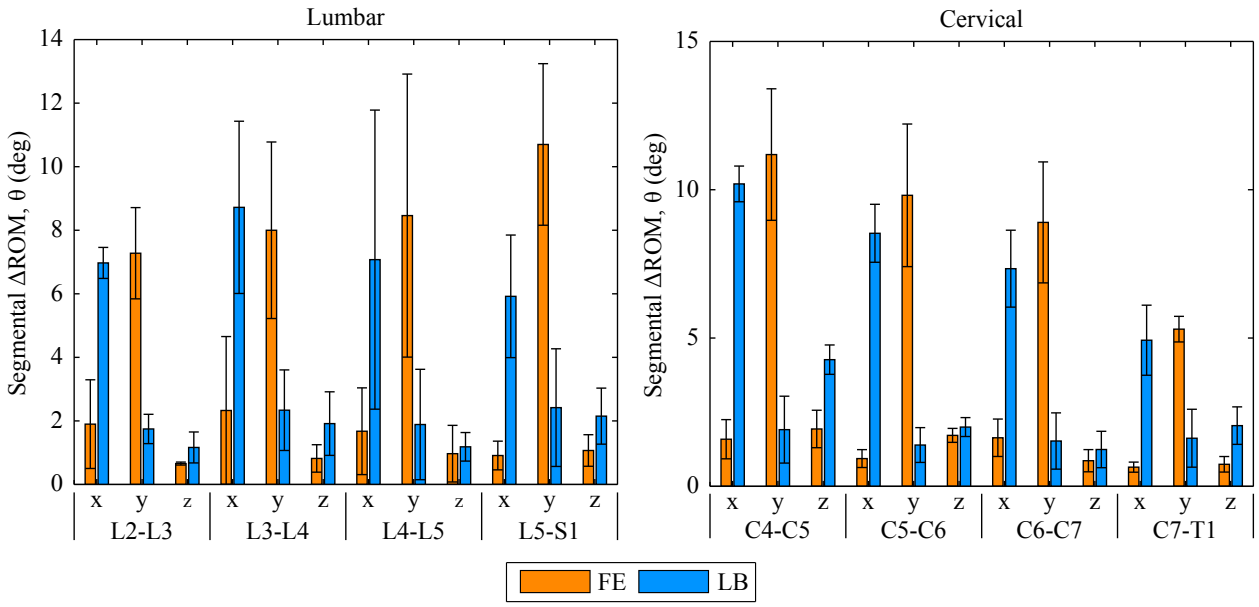

Figure 5.8: Dynamic assessment of the HAM-r during lumbar and cervical extension-to-flexion motion and left-to-right lateral bending motion using the Gold Standard 3-D CT-based specimen-specific model. There was statistically less variation in the motion about the primary axis for cervical specimen as oppose to lumbar specimen ($p < 0.05$, M = 1).

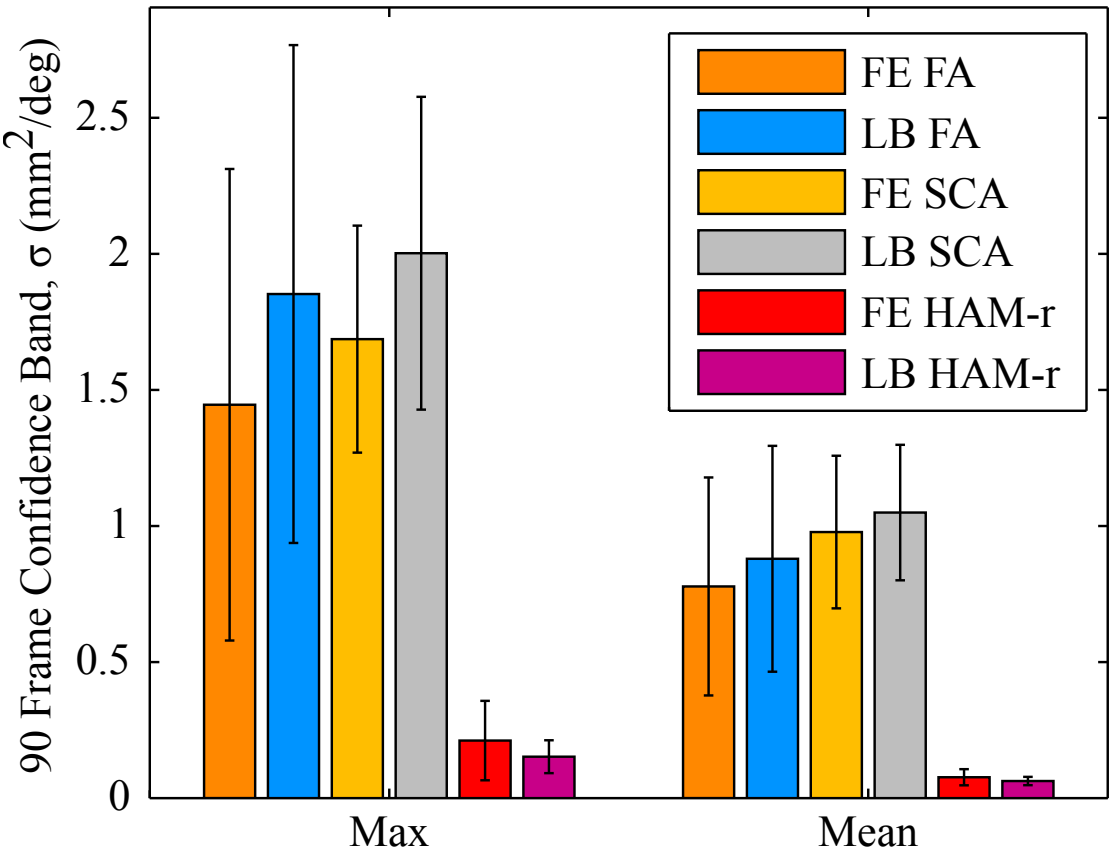

Figure 5.9: Noise in calculating the complex kinematic parameters FA, SCA, and HAM-r using the Gold Standard 3-D CT-based specimen-specific model. The flexion-extension and lateral bending motions of HAM-r had significantly less noise than all other parameters for both maximum and average noise values after normalizing with respect to the maximum change of the kinematic parameter ($p < 0.05$, M = 2).

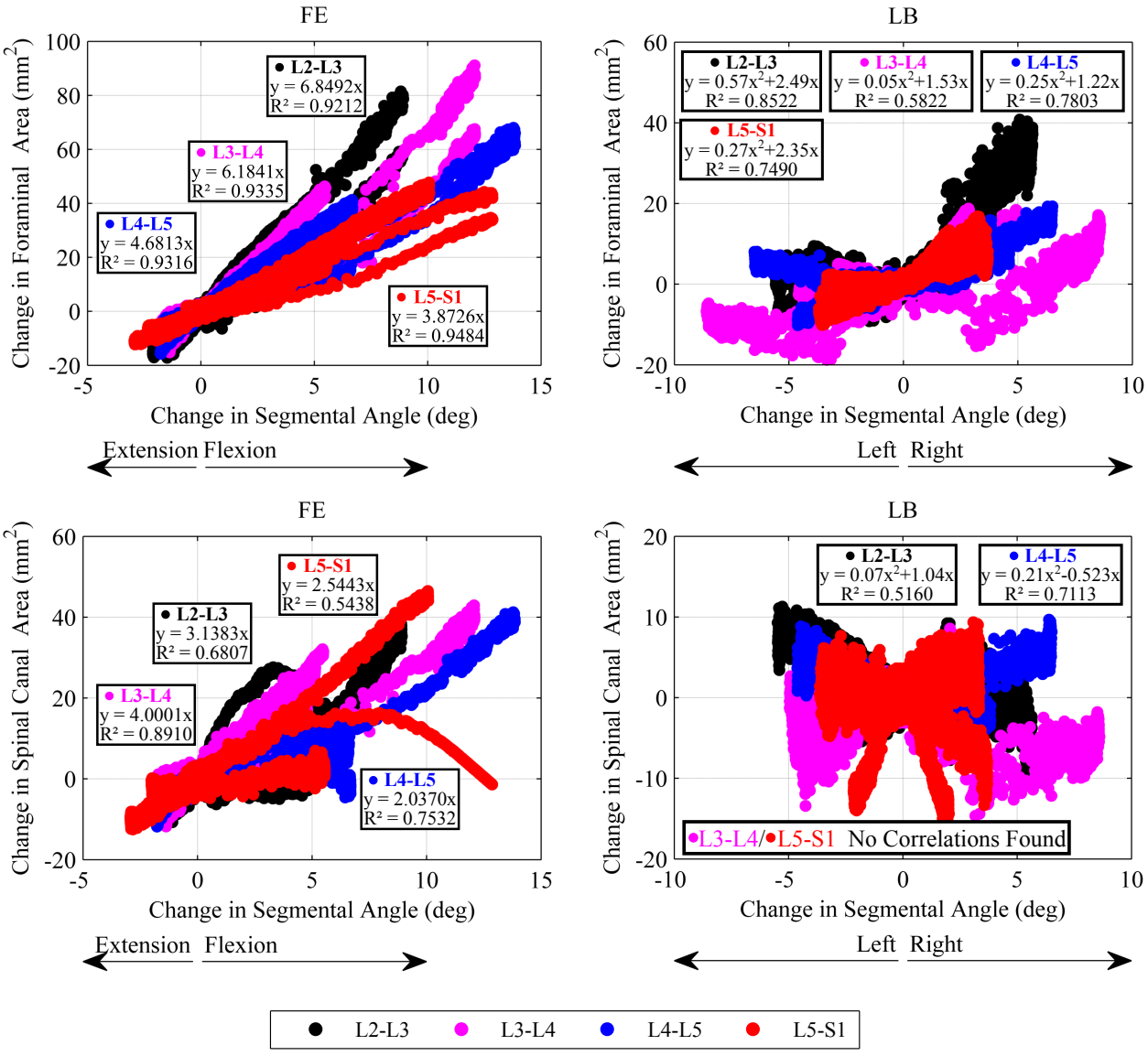

Figure 5.10: Correlation between the change in foraminal area and spinal canal area for each lumbar segmental joint of all specimen and its respective segmental motion change relative to the neutral posture. As motion moves from extension to flexion, foraminal area increases. Lateral bending foraminal area was flipped for the right foramen in order to overlay it on the left foramen.

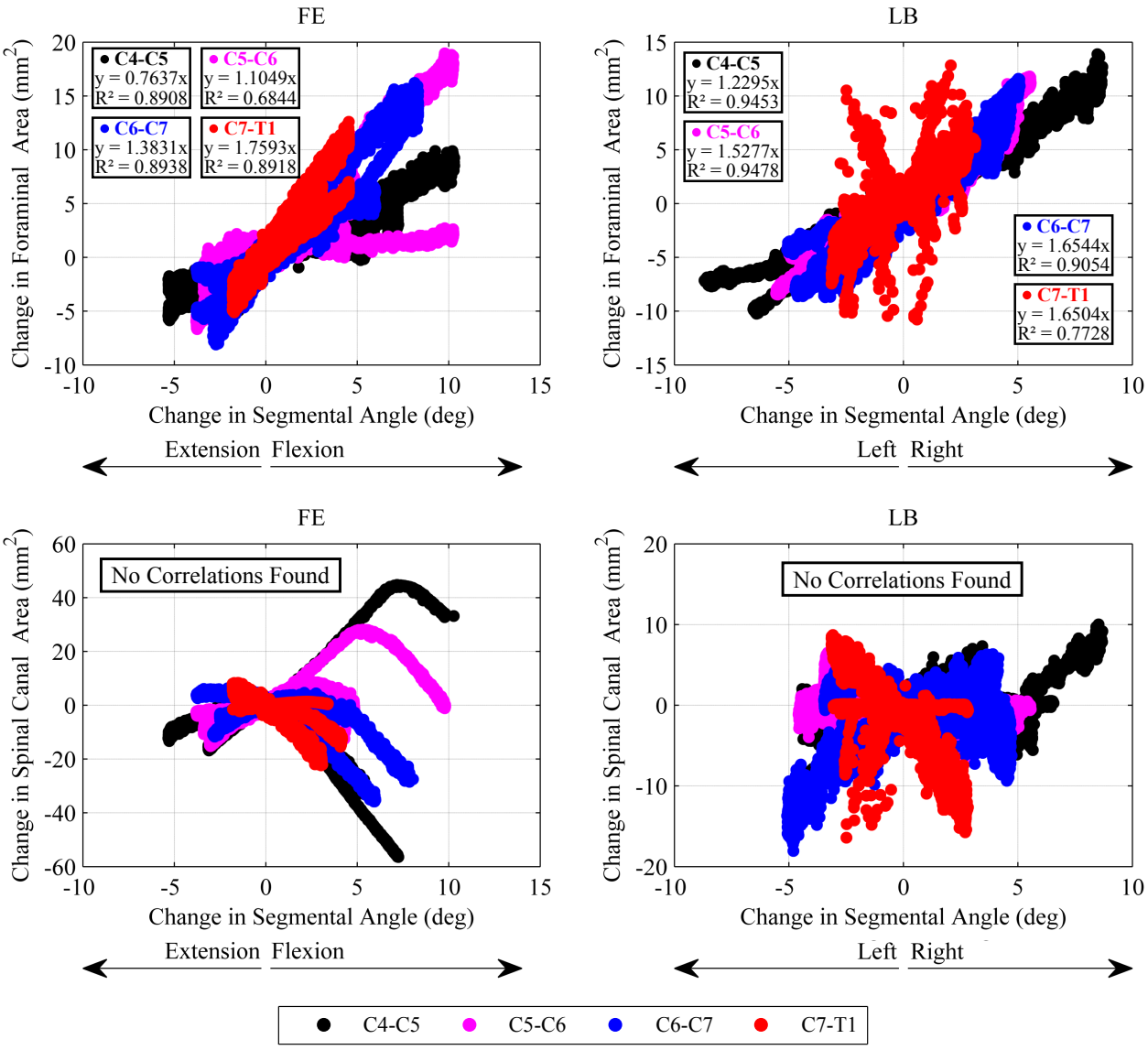

Figure 5.11: Correlation between the change in foraminal area and spinal canal area for each cervical segmental joint of all specimen and its respective segmental motion change relative to the neutral posture. As motion moves from extension to flexion, foraminal area increases. Lateral bending foraminal area was flipped for the right foramen in order to overlay it on the left foramen.

5.8 Tables

Table 5.1: Difference between the maximum error of the sampling point and the maximum error from interpolation.

		FA (mm^2)	HAM-r (deg)	SCA (mm^2)
Maximum Error	Mean	1.42	0.13	0.93
	STD Dev	2.10	0.22	1.20
RMSE	Mean	1.11	0.13	0.82
	STD Dev	2.18	0.26	0.95

Table 5.2: Number of successful vertebral segment registration success with a sampling size of 9 of all specimen with respect to their kinematic parameters. Success is determined by an error value less than those in the columns 1-3.

Maximum Error Values			FE			LB		
FA (mm^2)	HAM-r (deg)	SCA (mm^2)	FA	HAM-r	SCA	FA	HAM-r	SCA
4.0	**1.2**	**6.0**	15	25	6	17	19	15
1.5	**0.5**	**3.0**	2	12	3	5	9	4

Table 5.3: RMS maximum and RMS average accuracy of sucessfully interpolated bi-planar registration kinematic data for cervical and lumbar spine with a sample size of 9. For each lumbar and cervical motion, only segments which had successful results for all three kinematic parameters were used.

Study		Max		Mean	
Motion	Parameter	Lumbar (FE, N = 4; LB, N = 5)	Cervical (FE, N = 4; LB, N = 7)	Lumbar (FE, N = 4; LB, N = 5)	Cervical (FE, N = 4; LB, N = 7)
FE	FA	4.59	1.83	2.59	0.85
	HAM-r	0.48	1.01	0.30	0.60
	SCA	3.14	7.22	1.61	3.97
LB	FA	4.49	3.30	2.27	1.25
	HAM-r	0.41	1.03	0.21	0.52
	SCA	5.58	5.39	2.32	2.61

Table 5.4: Cervical foraminal and spinal canal area (mm^2) in the neutral posture projected onto the plane which maximized its area.

Parameter	C4-C5	C5-C6	C6-C7	C7-T1
FA (mm^2)	41.6 ± 4.7	46.4 ± 6.2	51.1 ± 4.3	50.1 ± 10.7
SCA (mm^2)	255.1 ± 13.6	265.8 ± 27.9	268.0 ± 30.6	266.5 ± 37.6

Table 5.5: Lumbar foraminal and spinal canal area (mm^2) in the neutral posture projected onto the plane which maximized its area.

Parameter	L2-L3	L3-L4	L4-L5	L5-S1
FA (mm^2)	126.1 ± 22.3	119.2 ± 25.0	100.9 ± 28	115.6 ± 11.6
SCA (mm^2)	215.4 ± 36.0	199.8 ± 39.5	227.0 ± 60.1	265.5 ± 93.4

Table 5.6: Statistical correlation between the best fit linear equation to the cervical spine kinematic parameters FA and SCA as a function of segmental angle for all cervical specimen.

Cervical					
		FA			
		C4-C5	C5-C6	C6-C7	C7-T1
FE	EQ	0.76x	1.10x	1.38x	1.76x
	R^2	0.89	0.68	0.89	0.89
LB	EQ	1.23x	1.53x	1.65x	1.65x
	R^2	0.95	0.95	0.91	0.77
		SCA			
		C4-C5	C5-C6	C6-C7	C7-T1
FE	EQ	-0.39x	1.14x	-2.69x	-2.19x
	R^2	-0.13	0.32	0.39	0.30
LB	EQ	0.49x	-0.28x	0.70x	-1.92x
	R^2	0.23	0.20	0.02	0.31

Table 5.7: Statistical correlation between the best fit linear or quadratic equation to the lumbar spine kinematic parameters FA and SCA as a function of segmental angle for all lumbar specimen.

Lumbar					
		FA			
		L2-L3	L3-L4	L4-L5	L5-S1
FE	EQ	6.85x	6.18x	4.68x	3.83x
	R^2	0.92	0.93	0.93	0.95
LB	EQ	$0.57x^2+2.49x$	$0.05x^2+1.53x$	$0.25x^2+1.22x$	$0.27x^2+2.35x$
	R^2	0.85	0.58	0.78	0.75
		SCA			
		L2-L3	L3-L4	L4-L5	L5-S1
FE	EQ	3.14x	4.00x	2.04x	2.54x
	R^2	0.68	0.89	0.75	0.54
LB	EQ	$0.07x^2+-1.04x$	$-0.11x^2+0.32x$	$0.21x^2+-0.52x$	$-0.25x^2+-0.62x$
	R^2	0.52	0.34	0.71	0.00

Chapter 6

Conclusions and Future Work

Patient-specific diagnostic techniques were evaluated in this dissertation. The conclusions founded by this work and the future work which needs to be considered is summarized.

6.1 Conclusions

The focus of this dissertation was upon improving in vivo diagnostic techniques for evaluating skeletal kinematics, more specifically the spine. Achievement of this goal required the (1) development of a new 3-D kinematic interpolation algorithm, (2) the development of a robust, non-invasive in vivo kinematic assessment procedure utilizing tools that could be readily available to clinicians; and (3) extending the non-invasive in vivo kinematic technique to acquire continuous 3-D kinematic data without excessive radiation. As a result, several contributions were made throughout the duration of this work.

6.1.1 Development of a New 3-D Kinematic Interpolation Algorithm

Extrapolating from quaternion interpolation techniques a new 3-D kinematic interpolation algorithm was derived from dual-quaternions. The dual-quaternion algorithm improved upon the accuracy of previous techniques and allowed for a reduction in the necessary number of x-rays taken to acquire a continuous bi-planar kinematic dataset. Additionally, the algorithm provided an automated method to handle non-uniform sampling for interpolation which were temporal in nature. Sampling which equally spaced out angular movement throughout the specimen's ROM provided the robust accuracy with a low sample size effectively minimizing radiation exposure. This was shown to be further optimizable by spacing sampling relative to known spinal features such as the high flexibility zone.

The new 3-D kinematic interpolation algorithm was proven to successfully reconstruct a continuous kinematic dataset describing spine-specific kinematic parameters illustrating its applicability to interpolate discontinuous bi-planar kinematic datasets.

6.1.2 Development of a Robust, Non-invasive In Vivo Kinematic Assessment Procedure

A clinically viable bi-planar fluoroscopic registration technique was developed utilizing clinically available fluoroscopic equipment, a 3-D printed calibration cube for fluoroscopic equipment registration, and custom written MATLAB scripts. Using bi-planar fluoroscopic images in combination with a reconstructed 3-D volume ('model') of the specimen, movement of the spine was tracked discretely. Bi-planar registration was achieved using a gradient derived objective function and a stochastic optimization function which reduced acquiring local minimums. Accuracy of the system was assessed using a previously developed ex vivo kinematic assessment technique. Reconstruction of the helical axis of motion, foraminal area, and spinal canal area was the basis for evaluating accuracy. Unfortunately, using the ex vivo technique for comparison introduced occlusions into the bi-planar radiographs, potentially reduced the accuracy of the bi-planar registration algorithm. Despite the reduced accuracy, a subset of specimen did achieve strong agreement with the Gold Standard technique.

6.1.3 Producing Continuous 3-D In Vivo Kinematics without Excessive Radiation

Results allude to the applicability of the specimen-specific CT-based model using bi-planar registration in combination with the new 3-D kinematic interpolation algorithm. Accuracy of interpolated results were bounded by the success of bi-planar registration. Provided accurate bi-planar registration results, the combination would produce a strong agreement with the Gold Standard technique which in conjunction with the patient's 3-D anatomic model, allow for a dynamic assessment of spine kinematic parameters and morphological interactions. For these cases, a sample size 8 (16 x-rays) was used to achieve strong accuracy for lumbar and cervical specimen. This is a dramatic reduction in compared to existing techniques which acquire from 120-180 x-rays for a single experiment to produce a continuous kinematic dataset.

6.1.4 Publications and Additional Contributions

The specimen-specific CT-based Gold Standard kinematic technique was verified and published in *Spine* [34]. The manuscript was the first study detailing the effects of FE motion on lumbar foraminal area.

The new 3-D kinematic interpolation algorithm was verified and published in the *Journal of Biomechanics* [25].

6.2 Future Work

Several questions and limitations of these experiments still need to be addressed. Additionally, manuscripts regarding these topics have yet to be submitted for publication.

6.2.1 Bi-planar Registration

Improvement of the bi-planar registration algorithm needs further investigation. For instance, in the current technique, the CT-scan was not segmented for each vertebrae when registering to the bi-planar dataset. Non-segmentation may introduce error since the vertebrae in the CT-scan are rigidly fixed which is not the case in the bi-planar dataset. Altering the objective function to include intensity measures as oppose to solely gradient based measurements or motion tracking constraints based upon the registration of prior and subsequent frames also needs further investigation.

Bi-planar registration success could be evaluated with respect to the radiopaque spheres implanted on each specimen in addition to the Gold Standard validation. Using the radiopaque spheres to evaluate success would indicate whether or not the best achievable registration could produce accurate results using the current procedure.

Ultimately, the final goal of this work is to complete clinical trials followed by making the technique clinically available for patient-specific diagnostics and evaluation of restorative technologies.

6.2.2 Publications

The new 3-D kinematic interpolation algorithm was proven to successfully reconstruct a continuous kinematic dataset describing spine-specific kinematic parameters illustrating its applicability to in-

terpolate discontinuous bi-planar kinematic datasets. A manuscript detailing this accomplishment will be submitted to the ASME *Journal of Biomechanical Engineering*.

After revision of the bi-planar registration algorithm, a manuscript describing the potential of interpolating bi-planar registration data will be investigated for submission.

References

[1] William Anderst, Emma Baillargeon, William Donaldson, Joon Lee, and James Kang. Motion Path of the Instant Center of Rotation in the Cervical Spine During In Vivo Dynamic Flexion-Extension: Implications for Artificial Disc Design and Evaluation of Motion Quality Following Arthrodesis. *Spine (phila PA 1976)*, 38(10):E594–E601, 2013.

[2] William Anderst, William Donaldson, Joon Lee, and James Kang. Cervical disc deformation during flexion-extension in asymptomatic controls and single-level arthrodesis patients. *Journal of orthopaedic research : official publication of the Orthopaedic Research Society*, 31(12):1881–9, 2013.

[3] William J. Anderst. Functional Movement. *Computer Methods in Biomechanics and Biomedical Engineering*, (January):1–9, 2011.

[4] William J Anderst, Emma Baillargeon, William F Donaldson, Joon Y Lee, and James D Kang. Validation of a noninvasive technique to precisely measure in vivo three-dimensional cervical spine movement. *Spine*, 36(6):E393–400, 2011.

[5] William J Anderst, William F Donaldson, Joon Y Lee, and James D Kang. Cervical Motion Segment Percent Contributions to Flexion-Extension during Continuous Movement in Control Subjects and Arthrodesis Patients. *Spine (phila PA 1976)*, 38(9):E533–E539, 2013.

[6] William J. Anderst, William F. Donaldson, Joon Y. Lee, and James D. Kang. Three-dimensional intervertebral kinematics in the healthy young adult cervical spine during dynamic functional loading. *Journal of Biomechanics*, 48(7):1286–1293, 2015.

[7] William J. Anderst, Joon Y. Lee, William F. III Donaldson, and James D. Kang. Six-Degrees-of-Freedom Cervical Spine Range of Motion During Dynamic Flexion-Extension After Single-Level Anterior Arthrodesis. *Journal of Bone and Joint Surgery*, 95(6):497–506, 2013.

[8] L. Blankevoort, R. Huiskes, and A. De Lange. Helical axes of passive knee joint motions. *Journal of Biomechanics*, 23(12):1219–1229, 1990.

[9] S D Boden, D O Davis, T S Dina, N J Patronas, S W Wiesel, J Bone Joint, and Surg Am. Abnormal magnetic-resonance scans of the lumbar spine in asymptomatic subjects . A prospective investigation Abnormal Lumbar Magnetic-Resonance Spine Scans of the in Asymptomatic. *Journal of Bone and Joint Surgery*, 72(3):403–408, 1990.

[10] S D Boden, P R McCowin, D O Davis, T S Dina, A S Mark, and S Wiesel. Abnormal magnetic-resonance scans of the cervical spine in asymptomatic subjects. A prospective investigation. *The Journal of bone and joint surgery. American volume*, 72(8):1178–84, sep 1990.

[11] James Coburn and Joseph J Crisco. Interpolating three-dimensional kinematic data using quaternion splines and hermite curves. *Journal of biomechanical engineering*, 127(2):311–317, 2005.

[12] Pierre Côté, Gabrielle van der Velde, J. David Cassidy, Linda J. Carroll, Sheilah Hogg-Johnson, Lena W. Holm, Eugene J. Carragee, Scott Haldeman, Margareta Nordin, Eric L. Hurwitz, Jaime Guzman, and Paul M. Peloso. The Burden and Determinants of Neck Pain in Workers. *Journal of Manipulative and Physiological Therapeutics*, 32(2):S70–S86, 2009.

[13] Mathieu Cuchanski, Daniel Cook, Donald M. Whiting, and Boyle C. Cheng. Measurement of occlusion of the spinal canal and intervertebral foramen by intervertebral disc bulge. *SAS Journal*, 5(1):9–15, 2011.

[14] L Y Dai, Y K Xu, W M Zhang, and Z H Zhou. The effect of flexion-extension motion of the lumbar spine on the capacity of the spinal canal. An experimental study. *Spine*, 14(5):523–525, 1989.

[15] Erik B Dam, Martin Koch, and Martin Lillholm. Quaternions , interpolation and animation. Technical report, 1998.

[16] Kostas Daniilidis. Hand-eye calibration using dual quaternions. *Ijrr*, 18(3):286–298, 1999.

[17] George E. Ehrlich. Low back pain. *Bulletin of the World Health Organization*, 81(9):671–676, 2003.

[18] Arin M Ellingson, Hitesh Mehta, David W Polly, Jutta Ellermann, and David J Nuckley. Disc degeneration assessed by quantitative T2* (T2 star) correlated with functional lumbar mechanics. *Spine*, 38(24):E1533–40, 2013.

[19] Arin M. Ellingson and David J. Nuckley. Altered helical axis patterns of the lumbar spine indicate increased instability with disc degeneration. *Journal of Biomechanics*, 48(2):361–369, 2015.

[20] Louis C. Fielding, Todd F. Alamin, Leonard I. Voronov, Gerard Carandang, Robert M. Havey, and Avinash G. Patwardhan. Parametric and cadaveric models of lumbar flexion instability and flexion restricting dynamic stabilization system. *European Spine Journal*, 22(12):2710–2718, 2013.

[21] a Fujiwara, T H Lim, H S An, N Tanaka, C H Jeon, G B Andersson, and V M Haughton. The effect of disc degeneration and facet joint osteoarthritis on the segmental flexibility of the lumbar spine. *Spine*, 25(23):3036–3044, 2000.

[22] J L Gaffey, A J Ghanayem, M L Voronov, R M Havey, G Carandang, C Abjornson, and A G Patwardhan. Effect of Increasing Implant Height on Lumbar Spine Kinematics and Foraminal Size Using the ProDisc-L Prosthesis. *Spine*, 35(19):1777–1782, 2010.

[23] Luciana Gazzi, Anna Bodnar, and Michele C Battié. A comparison of two methods to evaluate a narrow spinal canal : routine magnetic resonance imaging versus three-dimensional reconstruction. *The Spine Journal*, 16(7):884–888, 2016.

[24] Q. J. Ge and B. Ravani. Computer aided geometric design of motion interpolants. *Journal of Mechanical Design*, 116(3):756, 1994.

[25] Jeremy E. Goodsitt, Robert M. Havey, Saeed Khayatzadeh, Leonard I. Voronov, and Avinash G. Patwardhan. Interpolation of three Dimensional Kinematics with Dual-quaternions. *Journal of Biomechanics*, oct 2016.

[26] Mahmoud Gouasmi. Robot kinematics, using dual quaternions. *IAES International Journal of Robotics and Automation (IJRA)*, 1(1), 2012.

[27] William Rowan Hamilton. On quaternions; or on a new system of imaginaries in algebra. *Philosophical Magazine Series 3*, 25(163):10–13, 1844.

[28] N Hansen and S Kern. Evaluating the CMA Evolution Strategy on Multimodal Test Functions. *Proceedings of the 8th International Conference on Parallel Problem Solving from Nature - PPSN VIII*, 3242/2004(0):282–291, 2004.

[29] H Hatze. High-precision three-dimensional photogrammetric calibration and object space reconstruction using a modified dlt-approach. *Journal of biomechanics*, 6(May 1987):129–135, 1988.

[30] R Havey, J Goodsitt, T Potluri, S Hannon, B McIntosh, F Phillips, P Tsitsopoulos, L Voronov, and A Patwardhan. Specimen-Specific Model for Kinematic Assessment of Cervical Facet Joints. In *Orthopedic Research Society Annual Meeting*, San Francisco, CA, 2012.

[31] R Havey, J Goodsitt, T Potluri, S Hannon, B McIntosh, F Phillips, M Zindrick, P Tsitsopoulos, L Voronov, and A Patwardhan. Facet Engagement in the Intact Cervical Spine. In *International Society for the Advancement of Spine Surgery (ISASS) Annual Meeting*, Barcelona, Spain, 2012.

[32] R Havey, T Potluri, J Goodsitt, S Hannon, L Voronov, B McIntosh, M Zindrick, F Phillips, P Tsitsopoulos, and A Patwardhan. Does disc arthroplasty alter cervical facet engagement? A combinatorial approach using experimental data and 3-D CT Model. In *Cervical Spine Research Society Annual Meeting*, Chicago, IL, 2012.

[33] Robert Havey, Tejaswy Potluri, L Voronov, P Tsitsopoulos, F Phillips, M Zindrick, J Goodsitt, and G Patwardhan Carandang. Assessment of neuroforaminal and canal dimensions during cervical kinematics. In *International Society for the Advancement of Spine Surgery (ISASS) Annual Meeting*, Vancouver, Canada, 2013.

[34] Robert M. Havey, Jeremy Goodsitt, Saeed Khayatzadeh, Muturi Muriuki, Tejaswy Potluri, Leonard I. Voronov, Laurie M. Lomasney, and Avinash G. Patwardhan. Three-dimensional computed tomography-based specimen-specific kinematic model for ex vivo assessment of lumbar neuroforaminal space. *Spine*, 40(14):E814–E822, 2015.

[35] Charles G. Helmick, David T. Felson, Reva C. Lawrence, Sherine Gabriel, Rosemarie Hirsch, C. Kent Kwoh, Matthew H. Liang, Hilal Maradit Kremers, Maureen D. Mayes, Peter A. Merkel, Stanley R. Pillemer, John D. Reveille, and John H. Stone. Estimates of the prevalence of arthritis and other rheumatic conditions in the United States. Part I. *Arthritis and Rheumatism*, 58(1):15–25, 2008.

[36] Sheilah Hogg-Johnson, Gabrielle van der Velde, Linda J. Carroll, Lena W. Holm, J. David Cassidy, Jamie Guzman, Pierre Côté, Scott Haldeman, Carlo Ammendolia, Eugene Carragee, Eric Hurwitz, Margareta Nordin, and Paul Peloso. The Burden and Determinants of Neck Pain in the General Population. Results of the Bone and Joint Decade 2000-2010 Task Force on Neck Pain and Its Associated Disorders. *Journal of Manipulative and Physiological Therapeutics*, 32(2 SUPPL.):S46–S60, 2009.

[37] Ben Kenwright. A Beginners Guide to Dual-Quaternions: What They Are, How They Work, and How to Use Them for 3D Character Hierarchies. *The 20th International Conference on Computer Graphics, Visualization and Computer Vision*, pages 1–13, 2012.

[38] H-Y Ko, J H Park, Y B Shin, and S Y Baek. Gross quantitative measurements of spinal cord segments in human. *Spinal cord*, 42(1):35–40, 2004.

[39] Doris H. U. Kochanek and Richard H. Bartels. Interpolating splines with local tension, continuity, and bias control. *ACM SIGGRAPH Computer Graphics*, 18(3):33–41, 1984.

[40] Michal Kozanek, Shaobai Wang, Peter G Passias, Qun Xia, Gang Li, Christopher M Bono, Kirkham B Wood, and Guoan Li. Range of motion and orientation of the lumbar facet joints in vivo. *Spine*, 34(19):E689–E696, 2009.

[41] S. C B Lam, Brendan McCane, and Robert Allen. Automated tracking in digitized videofluoroscopy sequences for spine kinematic analysis. *Image and Vision Computing*, 27(10):1555–1571, 2009.

[42] Sang-Hun Lee, Ki-Tack Kim, Kyung-Soo Suk, Jung-Hee Lee, Jae-Hung Shin, Dong-Hyuk So, and Yoon-Ho Kwack. Asymptomatic cervical cord compression in lumbar spinal stenosis patients: a whole spine magnetic resonance imaging study. *Spine*, 35(23):2057–63, 2010.

[43] Guoan Li, Shaobai Wang, Peter Passias, Qun Xia, Gang Li, and Kirkham Wood. Segmental in vivo vertebral motion during functional human lumbar spine activities. *European Spine Journal*, 18(7):1013–1021, 2009.

[44] Weishi Li, Shaobai Wang, Qun Xia, Peter Passias, Michal Kozanek, Kirkham Wood, and Guoan Li. Lumbar facet joint motion in patients with degenerative disc disease at affected and adjacent levels: an in vivo biomechanical study. *Spine*, 36(10):E629–E637, 2011.

[45] Vincent Y. Ma, Leighton Chan, and Kadir J. Carruthers. Incidence, prevalence, costs, and impact on disability of common conditions requiring rehabilitation in the united states: Stroke, spinal cord injury, traumatic brain injury, multiple sclerosis, osteoarthritis, rheumatoid arthritis, limb loss, and back pa. *Archives of Physical Medicine and Rehabilitation*, 95(5):986–995.e1, 2014.

[46] Haiqing Mao, Sean J. Driscoll, Jing Sheng Li, Guoan Li, Kirkham B. Wood, and Thomas D. Cha. Dimensional changes of the neuroforamina in subaxial cervical spine during in vivo dynamic flexion-extension. *Spine Journal*, 16(4):540–546, 2015.

[47] B I Martin, R A Deyo, S K Mirza, J A Turner, B A Comstock, W Hollingworth, and S D Sullivan. Expenditures and health status among adults with back and neck problems. *JAMA*, 299(6):656–664, 2008.

[48] Brendan McCane, Tamara I. King, and J. Haxby Abbott. Calculating the 2D motion of lumbar vertebrae using splines. *Journal of Biomechanics*, 39(14):2703–2708, 2006.

[49] João Levy Melancia, António Fernandes Francisco, and João Lobo Antunes. Spinal stenosis. *Handbook of Clinical Neurology*, 119:541–549, 2014.

[50] Jun Miao, Shaobai Wang, Won Man Park, Qun Xia, Xiutong Fang, Martin P. Torriani, Kirkham B. Wood, and Guoan Li. Segmental spinal canal volume in patients with degenerative spondylolisthesis. *Spine Journal*, 13(6):706–712, 2013.

[51] Thybout M. Moojen, Jeroen G. Snel, Marco J.P.F. Ritt, Henk W. Venema, John M.G. Kauer, and Kurt E. Bos. In vivo analysis of carpal kinematics and comparative review of the literature. *The Journal of Hand Surgery*, 28(1):81–87, 2003.

[52] Yoshito Otake, Mehran Armand, Robert S. Armiger, Michael D. Kutzer, Ehsan Basafa, Peter Kazanzides, and Russell H. Taylor. Intraoperative image-based multiview 2D/3D registration for image-Guided orthopaedic surgery: Incorporation of fiducial-Based C-Arm tracking and GPU-Acceleration. *IEEE Transactions on Medical Imaging*, 31(4):948–962, 2012.

[53] M M Panjabi. The stabilizing system of the spine. Part II. Neutral zone and instability hypothesis., 1992.

[54] M M Panjabi, V K Goel, and S D Walter. Errors in kinematic parameters of a planar joint: guidelines for optimal experimental design. *Journal of biomechanics*, 15(7):537–44, 1982.

[55] M M Panjabi, M H Krag, and V K Goel. A technique for measurement and description of three-dimensional six degree-of-freedom motion of a body joint with an application to the human spine. *Journal of biomechanics*, 14(1978):447–460, 1981.

[56] Peter G. Passias. Segmental Lumbar Rotation in Patients with Discogenic Low Back Pain During Functional Weight-Bearing Activities. *The Journal of Bone and Joint Surgery (American)*, 93(1):29, 2011.

[57] a G Patwardhan, a Rimkus, T M Gavin, M Bueche, K P Meade, R Bielski, and K Ibrahim. Geometric analysis of coronal decompensation in idiopathic scoliosis., 1996.

[58] Lucas JW Pleis JR, Ward BW. Summary Health Statistics for U.S. adults: national health interview survey, 2009. Vital and health statistics. *National Health Interview Survey*, 10:1–207, 2009.

[59] Tomislav Pribanic. Matlab function for 3-D camera calibration using the modified DLT method., 1999.

[60] N S Schonstrom, N F Bolender, and D M Spengler. The pathomorphology of spinal stenosis as seen on CT scans of the lumbar spine., 1985.

[61] Boris Peter Selby, Georgios Sakas, Wolfgang Dieter Groch, and Uwe Stilla. Patient positioning with X-ray detector self-calibration for image guided therapy. *Australasian Physical and Engineering Sciences in Medicine*, 34(3):391–400, 2011.

[62] Volker K H Sonntag. The asymptomatic degenerative cervical disc: A dilemma. *World Neurosurgery*, 78(3-4):241–242, 2012.

[63] I A Stokes. Bulging of lumbar intervertebral discs: non-contacting measurements of anatomical specimens. *J Spinal Disord*, 1(3):189–193, 1988.

[64] Dean K. Stolworthy, Shannon a. Zirbel, Larry L. Howell, Marina Samuels, and Anton E. Bowden. Characterization and prediction of rate-dependent flexibility in lumbar spine biomechanics at room and body temperature. *The Spine Journal*, 14(5):789–798, 2014.

[65] Jefry Tedjokusumo and Wee Kheng Leow. Normalization and Alignment of 3D Objects Based on Bilateral Symmetry Planes. In *Advances in Multimedia Modeling, 13th International Multimedia Modeling Conference, {MMM} 2007, Singapore, January 9-12, 2007. Proceedings, Part {I}*, pages 74–85, 2007.

[66] Fuat Torun, Habibullah Dolgun, Hakan Tuna, Ayhan Attar, Aylin Uz, and Atilla Erdem. Morphometric analysis of the roots and neural foramina of the lumbar vertebrae. *Surgical Neurology*, 66(2):148–151, 2006.

[67] Shaobai Wang, Peter Passias, Gang Li, Guoan Li, and Kirkham Wood. Measurement of vertebral kinematics using noninvasive image matching method-validation and application. *Spine*, 33(11):E355–E361, 2008.

[68] Shaobai Wang, Qun Xia, Peter Passias, Weishi Li, Kirkham Wood, and Guoan Li. How does lumbar degenerative disc disease affect the disc deformation at the cephalic levels in vivo? *Spine*, 36(9):E574–E581, 2011.

[69] J U Yoo, D Zou, W T Edwards, J Bayley, and H a Yuan. Effect of cervical spine motion on the neuroforaminal dimensions of human cervical spine., oct 1992.